



# Morphology, Activation, and Metal Substitution Effects of $\text{AlPO}_4\text{-5}$ for $\text{CO}_2$ Pressure Swing Adsorption

Andreas Papageorgiou<sup>1,2</sup>, K. Suresh Kumar Reddy<sup>1</sup>, Dimitrios Karonis<sup>2</sup>, Donald Reinalda<sup>1</sup>, Yasser Al Wahedi<sup>1,3</sup> and Georgios N. Karanikolos<sup>1,3,4\*</sup>

<sup>1</sup> Department of Chemical Engineering, Khalifa University, Abu Dhabi, United Arab Emirates, <sup>2</sup> School of Chemical Engineering, National Technical University of Athens, Athens, Greece, <sup>3</sup> Center for Catalysis and Separations (CeCaS), Khalifa University, Abu Dhabi, United Arab Emirates, <sup>4</sup> Research and Innovation Center on  $\text{CO}_2$  and  $\text{H}_2$  (RICH), Khalifa University, Abu Dhabi, United Arab Emirates

Aluminophosphate,  $\text{AlPO}_4\text{-5}$ , an AFI zeotype framework consisting of one-dimensional parallel micropores, and metal-substituted  $\text{AlPO}_4\text{-5}$  were prepared and studied for  $\text{CO}_2$  adsorption. Preparation of  $\text{AlPO}_4\text{-5}$  by using different activation methods (calcination and pyrolysis), incorporation of different metals/ions (Fe, Mg, Co, and Si) into the framework using various concentrations, and manipulation of the reaction mixture dilution rate and resulting crystal morphology were examined in relation to the  $\text{CO}_2$  adsorption performance. Among the various metal-substituted analogs, FeAPO-5 was found to exhibit the highest  $\text{CO}_2$  capacity at all pressures tested (up to 4 bar). Among the Fe-substituted samples,  $x\text{FeAPO-5}$ , with  $x$  being the  $\text{Fe}/\text{Al}_2\text{O}_3$  molar ratio in the synthesis mixture (range of 2.5:100–10:100), 5FeAPO-5 exhibited the highest capacity (1.8 mmol/g at 4 bar, 25°C) with an isosteric heat of adsorption of 23 kJ/mol for 0.08–0.36 mmol/g of  $\text{CO}_2$  loading. This sample also contained the minimum portion of extra-framework or clustered iron and the highest mesoporosity. Low water content in the synthesis gel led to the formation of spherical agglomerates of small 2D-like crystallites that exhibited higher adsorption capacity compared to columnar-like crystals produced by employing more dilute mixtures.  $\text{CO}_2$  adsorption kinetics was found to follow a pseudo-first-order model. The robust nature of  $\text{AlPO}_4\text{-5}$ -based adsorbents, their unique one-dimensional pore configuration, fast kinetics, and low heat of adsorption make them promising for pressure swing adsorption of  $\text{CO}_2$  at industrial scale.

**Keywords:** aluminophosphates, adsorption, carbon dioxide, AFI, metal substitution, zeolites, adsorption kinetics, PSA

## INTRODUCTION

The severe environmental concern related to the greenhouse effects is mainly attributed to gases that absorb and emit radiation within the thermal infrared range. The primary greenhouse gases are carbon dioxide, methane, water vapor, nitrous oxide, and ozone.  $\text{CO}_2$  is the most important contributor coming mainly from combustion of fossil fuels and being released into the atmosphere from the power plants, steel plants, cement industry, and other large-scale industrial operations, as well as from transportation (Kontos et al., 2014). Notably, the increase of total primary energy supply, reaching 150% in 2014 compared to 1971, is caused by the associated worldwide economic

## OPEN ACCESS

### Edited by:

Svetlana Ivanova,  
University of Seville, Spain

### Reviewed by:

Cristina Megías-Sayago,  
Université de Strasbourg, France  
Laura Pastor-Pérez,  
University of Surrey, United Kingdom

### \*Correspondence:

Georgios N. Karanikolos  
georgios.karanikolos@ku.ac.ae

### Specialty section:

This article was submitted to  
Green and Sustainable Chemistry,  
a section of the journal  
Frontiers in Chemistry

Received: 01 June 2020

Accepted: 24 August 2020

Published: 06 October 2020

### Citation:

Papageorgiou A, Reddy KSK,  
Karonis D, Reinalda D, Al Wahedi Y  
and Karanikolos GN (2020)  
Morphology, Activation, and Metal  
Substitution Effects of  $\text{AlPO}_4\text{-5}$  for  
 $\text{CO}_2$  Pressure Swing Adsorption.  
Front. Chem. 8:568669.  
doi: 10.3389/fchem.2020.568669

growth with fossil fuels holding the most significant share for that energy produced (Metz et al., 2005; IEA, 2016; Tabish et al., 2020). Under these circumstances, it is evident that carbon dioxide emissions will keep increasing as energy demands will continue being covered primarily by fossil fuels at least for the next 50 years.

CO<sub>2</sub> capture, utilization, and storage (CCUS) technologies have been proposed to stabilize the concentrations of greenhouse gases in the atmosphere and mitigate their impact. Among other proposed solutions, such as retrofits of existing units, usage of fuels with less carbon dioxide footprint, and nuclear and renewable energy, CCUS is the most promising one in terms of compatibility with the energy production, continued dependence on fossil fuels, and delivery infrastructure. Focusing on postcombustion, different technologies have been used. Employing amine-based solvents is the most mature technology. Monoethanolamine, diethanolamine, and *N*-methyldiethanolamine are commonly used alkanolamines. These lean amines, commonly diluted along with water of content in the order of about 70%, have a high reactivity toward CO<sub>2</sub>. Still, the technology has certain drawbacks mainly associated with high energy consumption for the regeneration step, requirement of large voluminous equipment, high corrosion rates, and solvents slippage to the atmosphere (Resnik et al., 2004; Haszeldine, 2009). As promising alternatives to solvent-based systems, which have constituted the main industrial practice for several decades, technologies based on adsorption and membrane separation are gaining considerable attention (Pilatos et al., 2010; Labropoulos et al., 2015; Kueh et al., 2018). Concerning adsorption, emphasis is put on porous materials. These can be divided into two categories: (i) physical adsorbents, such as porous carbons, zeolites, and metal-organic frameworks, and (ii) chemical adsorbents, such as functionalized materials with surface agents such as amine moieties (Choi et al., 2009; Sayari et al., 2011; Pokhrel et al., 2018; Varghese and Karanikolos, 2020). In this front, various materials are being discovered and explored, yet a platform of suitable materials/systems to treat a wide range of industrial emissions at a large scale still remains a challenge. The reason is that multiple factors need to be met at the same time, i.e., adsorbents need to exhibit (i) high capacity; selectivity compared to other components such as NO<sub>x</sub>, SO<sub>2</sub>, and H<sub>2</sub>O vapor; fast adsorption/desorption kinetics; and low energy consumption; and (ii) chemical and thermal stability, sustainable performance for many cycles, low manufacturing cost, and mechanical robustness at large scale.

Zeolites have been studied for CO<sub>2</sub> capture, particularly involving dry CO<sub>2</sub>, based on their relatively high adsorption capacity (Chue et al., 1995; Sircar and Golden, 1995; Siriwardane et al., 2001; Chou and Chen, 2004), low-cost of production, and excellent thermal stability (Musyoka et al., 2015). Yet, due to polar zeolite surfaces, these materials are highly hydrophilic resulting in lower CO<sub>2</sub> capture capacity and selectivity and early saturation in the presence of moisture (Corma, 2003). To battle this problem, less hydrophilic zeolite-type materials need to be explored. Aluminophosphates (AlPOs) are among the most notable adsorbents for this duty. AlPOs were discovered in

1982 by Wilson and partners of Union Carbide (Wilson et al., 1982). The framework of AlPOs, such as AlPO<sub>4</sub>-5, consists of alternating Al<sup>3+</sup> and P<sup>5+</sup> connected by oxygen atoms (Wilson et al., 1982; Stoeger et al., 2012). The main feature is the charge neutrality of the framework, which occurs from the equal ratio of alumina to phosphorus (Al/P = 1). This constant ratio producing materials of a net neutral electric charge prevents ion exchange, and as a result, AlPOs tend to be only slightly hydrophilic due to the absence of acidic sites (Cundy and Cox, 2003; Carmine, 2012). Indeed, in our recent work, we showed that AlPO<sub>4</sub>-5 is rather hydrophobic particularly at relatively low water partial pressures, where water molecules occupy niches close to pore walls, followed later by the filling of the central pore area (Schlegel et al., 2018). However, AlPOs retain their CO<sub>2</sub> sorption capacity potential due to the high concentration of physisorption sites. Therefore, the limited hydrophilicity, concentration of physisorption sites, and more linear shape of the CO<sub>2</sub> adsorption isotherms as compared to other zeolites suggest that these materials would have a longer process lifetime extending over many adsorption/regeneration cycles by pressure-mediated tuning between adsorption/desorption cycles [pressure swing adsorption (PSA)]. Liu et al. (2011) examined 8-member ring AlPOs (AlPO<sub>4</sub>-17, AlPO<sub>4</sub>-18, AlPO<sub>4</sub>-53, and AlPO<sub>4</sub>-25) at different temperatures and determined CO<sub>2</sub> uptake capacities in the range of 1.52–2.32 mmol/g at 273–293 K and 100 kPa. Among the above structures, AlPO<sub>4</sub>-53 possessed a higher CO<sub>2</sub> affinity and a CO<sub>2</sub>/N<sub>2</sub> selectivity of 98.4 with low interaction with water molecules as compared to the benchmark zeolite 13X. Zhao et al. (2009) investigated AlPO<sub>4</sub>-14 and reported CO<sub>2</sub> adsorption capacities ranging from 2.0 to 2.7 mmol/g within the temperature range of 273–300 K at 100 kPa, exhibiting also relatively high CO<sub>2</sub> over CH<sub>4</sub> selectivity. Delgado et al. (2013) studied the adsorption behavior of AlPO<sub>4</sub>-11 for CO<sub>2</sub>, CH<sub>4</sub> and N<sub>2</sub> and reported a CO<sub>2</sub> adsorption capacity of 0.31–0.7 mmol/g at 298–338 K and 100 kPa.

In addition to high adsorption capacity and selectivity, fast adsorption/desorption kinetics and a low heat of adsorption are key factors for an industrially prominent adsorbent candidate in PSA CO<sub>2</sub> capture applications. The work reported herein studies the synthesis and modification/functionalization of AlPO<sub>4</sub>-5 and its metal substituted analogs as potential candidates for CO<sub>2</sub> capture. The crystal lattice of AlPO<sub>4</sub>-5 possesses a hexagonal symmetry and a monodirectional channel morphology extending along the *c*-axis. The main channels are created by 12-member rings of alternating tetrahedra of [AlO<sub>4</sub>]<sup>-</sup> and [PO<sub>4</sub>]<sup>+</sup> having a diameter of 7.2 Å (Rajic and Kaucic, 2002; Guo et al., 2005; Karanikolos et al., 2008). Here, we assess the impact of various factors on CO<sub>2</sub> sorption, namely, (a) the effect of various heteroatoms used in isomorphic substitution in the AlPO<sub>4</sub>-5 framework at varying concentrations, (b) the pore activation method and in particular the affinity of remnant carbon species present into the inner pore surface after structure-directing agent (SDA) removal by two different thermal treatment methods, i.e., partial oxidation and pyrolysis, and (c) the impact of AlPO<sub>4</sub>-5 crystal morphology and hydrothermal synthesis mixture composition and in particular the water content in the mixture.

## EXPERIMENTAL SECTION

### Materials

Aluminum isopropoxide (Merck), orthophosphoric acid (85% in H<sub>2</sub>O, Sigma Aldrich), and triethylamine (TEA, Merck) were

used as precursors for AlPO<sub>4</sub>-5 growth. Tetraethyl orthosilicate (Merck), magnesium chloride (Merck), cobalt (II) acetate tetrahydrate (98%, Sigma-Aldrich), and iron (III) nitrate non-hydrate (Merck) were used as metal precursors for the synthesis of the metal-substituted AlPOs (MeAPO-5).

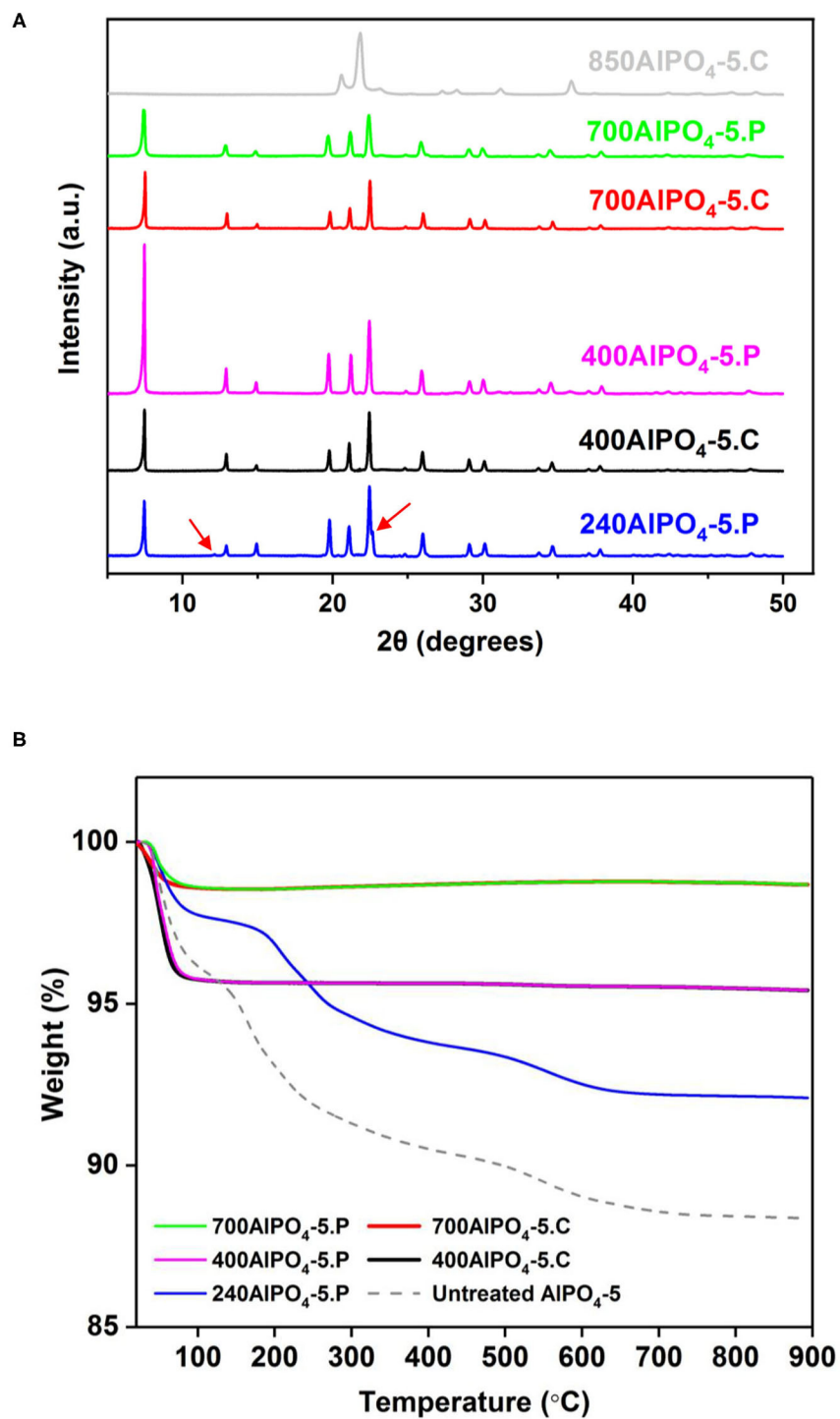


**FIGURE 1 | (A)** XRD patterns and **(B)** TGA profiles of calcined and pyrolyzed AlPO<sub>4</sub>-5 adsorbents treated at different temperatures.

## Growth of AlPO<sub>4</sub>-5 and MeAPO-5 Adsorbents

The AlPO materials were grown hydrothermally from reaction mixtures starting from a gel composition of 1Al<sub>2</sub>O<sub>3</sub>:1.3P<sub>2</sub>O<sub>5</sub>:1.2TEA:xMe:yH<sub>2</sub>O, where *x* and *y* refer to the metal/Al<sub>2</sub>O<sub>3</sub> and water/Al<sub>2</sub>O<sub>3</sub> molar ratios, respectively. Desired amount of aluminum isopropoxide was dissolved in deionized water under stirring for 3 h. To this solution, orthophosphoric acid was added dropwise, and the mixture was stirred for another 1 h. TEA, as the SDA, was then added dropwise, and the mixture was stirred for 24 h. For the preparation of the metal or ion substituted AlPOs, the metal precursor was added right after the addition of the SDA. The reaction gel having a pH ranging from 5 to 6 was transferred to a Teflon-lined stainless steel autoclave and placed inside a preheated oven at a temperature of 160°C for 24 h. After growth, the autoclave was quenched, and the solid product was collected after repeated centrifugation/washing cycles. The obtained crystals were dried at 80°C for 6 h and were subsequently calcined in air using a ramping rate of 2.5°C/min until temperature reached 80°C, keeping temperature stable for 30 min there, and further increasing it up to 600°C, where it was kept constant for 5.5 h. Activation at various temperatures under air flow (calcination) or nitrogen (pyrolysis) in a tubular furnace was also performed in order to parametrically explore decomposition/removal of the SDA occluded into the pores using the above temperature ramping program. A water/Al<sub>2</sub>O<sub>3</sub> molar ratio of 100:1 was used in these experiments. The MeAPOs were synthesized using different metals/ions (Fe, Mg, Co, and Si) into the AlPO<sub>4</sub>-5 framework with water/Al<sub>2</sub>O<sub>3</sub> molar ratio of 100:1 and metal/Al<sub>2</sub>O<sub>3</sub> ratio of 5:100. For the FeAPO-5 adsorbents, additional metal contents were studied as well.

The following naming code of samples was applied throughout the various sets of experiments in this work:

For the activation set of experiments: TAlPO<sub>4</sub>-5.P and TAlPO<sub>4</sub>-5.C, where *T* is the thermal treatment temperature in °C, and P and C stand for pyrolysis under inert atmosphere and calcination under airflow, respectively.

For the metal substitution set of experiments: The molar ratios were placed ahead of the sample names. For example, 5FeAPO-5 indicates a metal/Al<sub>2</sub>O<sub>3</sub> ratio of 5:100.

For the experiments on varying water content in the synthesis mixture: The H<sub>2</sub>O/Al<sub>2</sub>O<sub>3</sub> molar ratio was placed ahead of the sample names. For example, 400AlPO<sub>4</sub>-5 indicates a H<sub>2</sub>O/Al<sub>2</sub>O<sub>3</sub> ratio of 400:1.

## Characterization

The crystallinity of the synthesized samples was investigated by X-ray diffraction (XRD) using a Panalytical X'Pert Pro Powder Diffractometer. A Cu-K $\alpha$  monochromatized radiation source with wavelength  $\lambda = 1.5406$  Å, power 40 kV, and current of 40 mA was utilized, and the scan speed was set to 0.02 degrees/s. Morphology evaluation was performed by scanning electron microscopy (SEM) using an FEI Quanta 200 microscope. Samples were placed on a carbon tape and were coated by gold to enhance the conductivity and to allow observation at 30 kV. Ultraviolet-visible diffuse reflectance spectroscopy (UV-Vis

DRS) of the adsorbents was recorded using a Varian Analytical Cary 5000 UV-Vis-NIR spectrometer, equipped with diffuse reflectance accessory used to record electronic spectra from 200 to 800 nm. Thermogravimetric analysis (TGA) was performed using TA instruments Trios V3.1 analyzer under 50 mL/min of air flow with a ramping rate of 10°C/min from 25 to 900°C. Fourier-transform infrared spectroscopy (FTIR) was carried out on a BRUKER TENSOR II series FTIR spectrometer with the aid of diamond attenuated total reflectance crystal, where thin sections of the samples were scanned in the wavenumber region of 4,000 to 400 cm<sup>-1</sup> with a resolution of 4 cm<sup>-1</sup> by undergoing 32 scans. Nitrogen adsorption-desorption analysis was performed at 77 K using a Micromeritics 3-Flex analyzer. Before the analysis, the samples were degassed at 220°C for 3 h. The surface area was determined by the Brunauer-Emmett-Teller (BET) method. Pore size distribution and pore volume were obtained by processing adsorption-desorption data using the Barrett, Joyner, Halenda (BJH) and Horvath-Kawazoe (HK) models via the MicroActive software.

**TABLE 1** | Characteristic TGA transitions and corresponding weight loss percentages for the various calcined and pyrolyzed AlPO<sub>4</sub>-5 adsorbents.

Adsorbent	% Weight loss up to 100°C (adsorbed water)	% Weight loss between 100 and 900°C (organic content)
700AlPO <sub>4</sub> -5.C	1.32	0.10
700AlPO <sub>4</sub> -5.P	1.32	0.07
400AlPO <sub>4</sub> -5.C	4.25	0.34
400AlPO <sub>4</sub> -5.P	4.24	0.35
240AlPO <sub>4</sub> -5.P	2.25	5.66
Untreated AlPO <sub>4</sub> -5	3.84	7.80

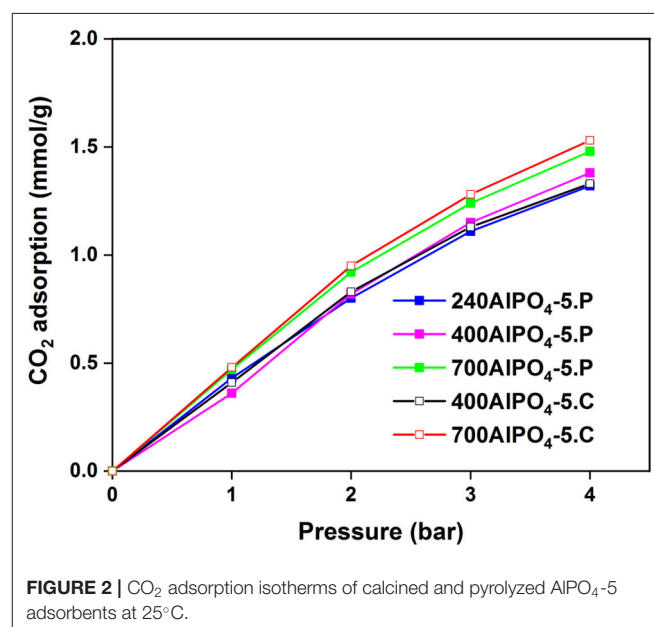


**FIGURE 2** | CO<sub>2</sub> adsorption isotherms of calcined and pyrolyzed AlPO<sub>4</sub>-5 adsorbents at 25°C.

## CO<sub>2</sub> Adsorption

CO<sub>2</sub> adsorption experiments were carried out using a Rubotherm gravimetric sorption analyzer (IsoSORP STATIC 3xV-MP). The magnetic suspension balance measures sample weight and gas dosing to determine the adsorption equilibrium. Approximately 50 mg of each activated adsorbent was first heated under vacuum at 150°C for 3 h to remove moisture and other volatile substances until a constant sample mass was obtained. Buoyancy correction was performed using helium gas and incorporated into the sample weight. The sample in a stainless-steel holder was pressurized with CO<sub>2</sub> gas up to 4 bar (in steps of 1 bar), and continuous measurement of sample mass gain during CO<sub>2</sub>

adsorption was determined at 25°C under equilibrium/saturation conditions. The gravimetric analyzer software uses the recorded mass changes to estimate the sorption capacity at each pressure step and incorporates the buoyancy correction as well in order to generate the final CO<sub>2</sub> sorption isotherm. For the adsorption kinetics study, the adsorbents were measured again but with a single step directly up to 4 bar taking capacity values at regular time intervals. The procedure was repeated for three different temperatures, namely, 25, 45, and 60°C.

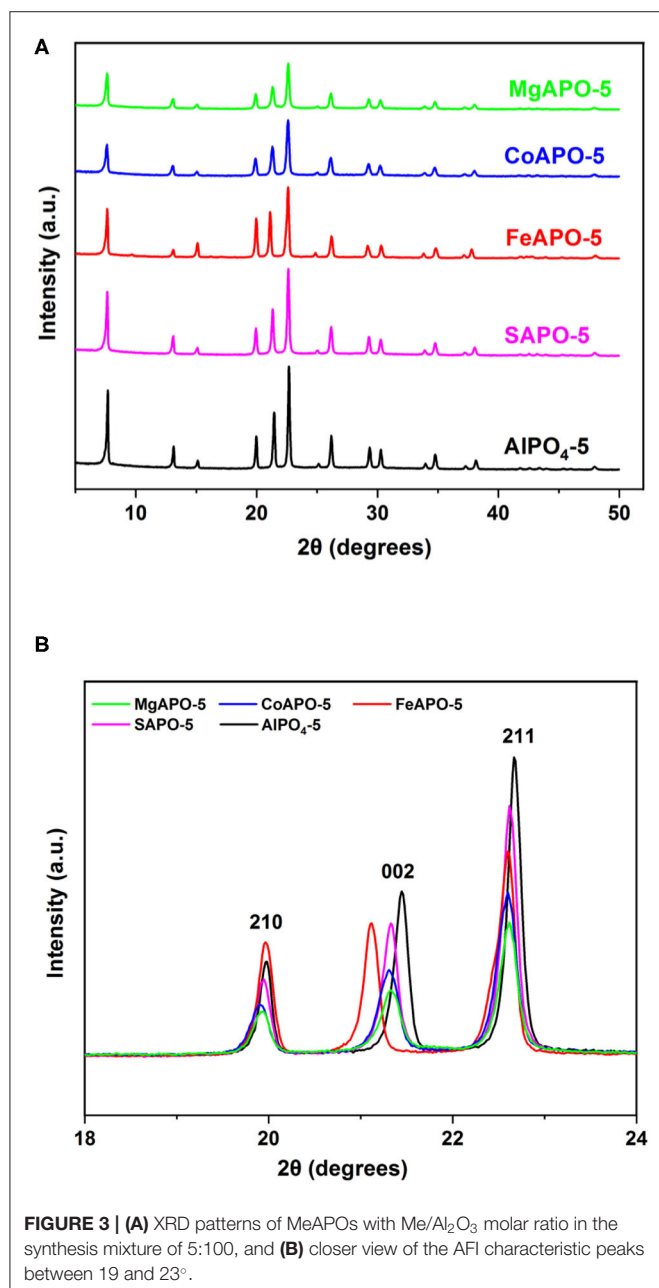
## RESULTS AND DISCUSSION

### Activation of Adsorbents by Calcination and Pyrolysis

Upon growth of porous crystalline materials such as zeolites, SDAs (or organic templates) are typically used to direct the formation of the pores. Following growth, removal of these molecules from the pores needs to take place as to activate the open porosity of the materials. Whether the occluded molecules are completely decomposed and removed or remnants of carbon still exist into the pores may affect the affinity and interaction of the internal surface with CO<sub>2</sub>. This was first investigated in our study by activating the resulting AlPO<sub>4</sub>-5 crystals via calcination and partial calcination (air flow) or pyrolysis (nitrogen atmosphere) at various temperatures. The latter was employed based on our previous work revealing that graphitic carbon in the form of carbon nanotubes (CNTs) into the pores of oriented AlPO<sub>4</sub>-5 films affected CO<sub>2</sub> sorption, as well as permeance behavior through the resulting CNT membranes (Labropoulos et al., 2015). In addition, the occluded amine SDA is partially decomposed and removed upon partial calcination, which might create extra spacing/porosity within the larger AlPO<sub>4</sub>-5 channels. The objective was to examine whether remaining carbon species would act favorably toward CO<sub>2</sub> adsorption via interaction of CO<sub>2</sub> with both AlPO<sub>4</sub>-5 and carbon surfaces, or complete removal of SDA would be preferred due to maximizing the pore volume and carbon-free AlPO<sub>4</sub>-5 surface.

Consequently, for calcination, five different temperatures were used, namely, 300, 400, 500, 600, and 700°C under airflow. The distinct color of the materials produced at the different calcination temperatures is shown in **Supplementary Figure 1**. The as-synthesized AlPO<sub>4</sub>-5 crystals had a white color. The material calcined between 300 and 500°C had a distinct brown coloration that turned softer as the temperature increased, which indicates the existence of remaining carbon species at the external crystal surface at these relatively low calcination temperatures with carbon content being decreased with increase in temperature. At temperatures above 600°C the materials turned white again, indicating complete carbon removal.

Pyrolysis of the synthesized AlPO<sub>4</sub>-5 samples was carried out under nitrogen flow at temperatures of 240, 400, and 700°C. The aim was to investigate possible affinity enhancement effects between CO<sub>2</sub> and carbon species resulting from the TEA pyrolysis in the pores or formation of additional carbon porosity/surface within the AFI channels. The creation of porous



carbon-based structure and possibly extra porosity inside the channels of AlPO<sub>4</sub>-5 might enhance affinity toward CO<sub>2</sub> due to the existence of pyrolytic carbon. Analogous treatment yielded

formation of single-wall CNTs inside the AFI pores of powder AlPO<sub>4</sub>-5 crystals (Tang et al., 1998), as well as in oriented membrane configuration for membrane-based gas separation, as

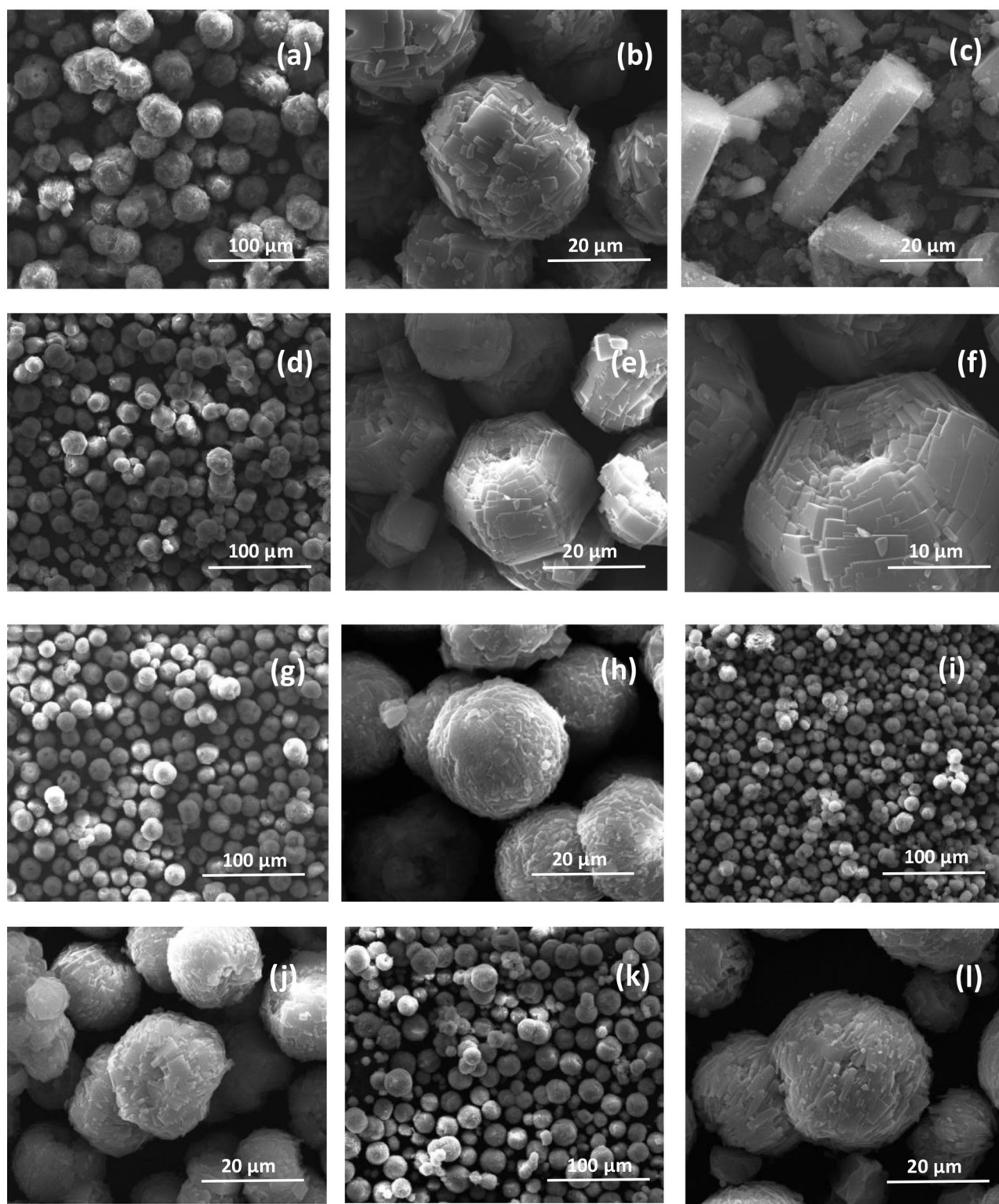


**FIGURE 4** | SEM images of (a,b) 100AlPO<sub>4</sub>-5, (c) 400AlPO<sub>4</sub>-5, (d-f) FeAPO-5, (g,h) MgAPO-5, (i,j) CoAPO-5, and (k,l) SAPO-5 adsorbents.

demonstrated in our previous work (Labropoulos et al., 2015). The pyrolysis temperature of 240°C was selected as it represents a point within the TEA decomposition region based on TGA data (Wan et al., 2000).

XRD analysis of selected calcined and pyrolyzed samples are shown in **Figure 1A**. The water/Al<sub>2</sub>O<sub>3</sub> molar ratio was fixed at 100 for this activation effect study. All samples treated at temperatures up to 700°C exhibit the characteristic diffraction peaks of AFI (Karanikolos et al., 2008; Basina et al., 2018), confirming the stability and structural integrity of the materials up to this temperature. Notably, the sample pyrolyzed at the lowest temperature (240°C), in addition to the AFI peaks, exhibits an additional peak shoulder at 22.6° and a minor peak at 12.1°, which are attributed to remnant carbon clusters (Sawant et al., 2017). At tested temperatures of 400°C and above, the above peaks disappear indicating that the remnant carbon content is significantly reduced or eliminated. Furthermore, such peaks do not exist in the untreated AlPO<sub>4</sub>-5 material either (**Supplementary Figure 2**). Thermal stability of a potential adsorbent is one of the key quality features for industrial application ensuring robustness upon thermal stresses that may occur during preparation as well as application. e.g., upon regeneration or other processing steps. The high temperature treatment applied here and the obtained stability of the AlPO<sub>4</sub>-5 adsorbents confirm their robustness and suitability for high temperature application. In order to explore the upper temperature stability limit, we also calcined the material at 850°C. There, we observed a structure collapse and transformation into a dense AlPO<sub>4</sub>-tridymite phase (Stoeger et al., 2012).

The carbon content of the thermally treated samples and their corresponding thermal behavior in comparison to untreated AlPO<sub>4</sub>-5 was further studied by TGA, which was performed under oxidative conditions (air). According to the obtained results (**Figure 1B**), the pyrolyzed and calcined adsorbents exhibit almost the same TGA profiles as revealed for the corresponding samples treated at 400 and 700°C. Notably, the only significant weight loss experienced by both of the above sets of samples is the one at the low temperature range of up to 100°C, which is attributed to removal of adsorbed moisture. The absence of any noticeable transition due to amine decomposition indicates that the occluded amine molecules have been almost completely removed from the pores at these temperatures. In addition, the samples treated at 700°C exhibit a more hydrophobic behavior containing 1.3 wt% of moisture compared to the ones treated at 400°C that contain approximately 4.2 wt% of moisture (**Table 1**). This is attributed to the fact that polar functional groups on the AlPO<sub>4</sub>-5 surface, such as Al-OH and P-OH (Peri, 1971), are being compromised by the higher temperature treatment, thus suppressing hydrophilicity. The untreated AlPO<sub>4</sub>-5 adsorbent and the one pyrolyzed at 240°C exhibit two distinct weight loss transitions after the removal of the adsorbed water. The first transition is attributed to decomposition of the TEA molecules from the pores and occurs in the temperature range of 120–300°C for the untreated sample, while it starts at a higher temperature (165°C) for the pyrolyzed one. This temperature difference is due to the fact that portion of the amine has already been decomposed in the latter

sample. The second transition occurs at a considerably higher temperature (500–650°C) and is attributed to the removal of trapped and possibly graphitized carbon species from the pores. As per **Table 1**, the total organic content in the untreated sample is 7.8 wt%, whereas that of the sample pyrolyzed at 240°C is 5.66 wt%. The existence of remnant carbon in the latter sample is in agreement to XRD evidence discussed above.

The effect of the calcination and pyrolysis treatment on the CO<sub>2</sub> adsorption capacity is depicted in **Figure 2** (data in **Supplementary Table 1**). The sample calcined at 700°C exhibits higher CO<sub>2</sub> capacity (1.53 mmol/g at 4 bar) than the one calcined at 400°C. This observation is consistent throughout the pressure range examined (up to 4 bar) and indicates that maximizing porosity in the channels of the adsorbent is critical. The sample pyrolyzed at 700°C exhibits higher CO<sub>2</sub> capacity compared to the other pyrolyzed samples throughout the pressure range of 0 to 4 bar, with a maximum capacity of 1.48 mmol/g at 4 bar. This is attributed to the total decomposition and removal of TEA from the framework, and the creation of clean pores in the zeolite to host the CO<sub>2</sub> molecules. The remaining two isotherms corresponding to the lower pyrolysis temperature samples (240AlPO<sub>4</sub>-5.P and 400AlPO<sub>4</sub>-5.P) are of interest since an inversion in the CO<sub>2</sub> adsorption capacity can be observed. Specifically, the sample which was treated at 240°C exhibits higher capacity at low pressures (up to 2 bar), whereas at higher pressures (2–4 bar) the sample treated at 400°C adsorbs more CO<sub>2</sub>. In addition, a noticeable observation with respect to low pressure CO<sub>2</sub> capture application is that, up to 1 bar, the sample pyrolyzed at 240°C exhibits almost same capacity as the one pyrolyzed at the highest temperature tested, i.e., 700°C, which is also very close to the capacity observed for the calcined sample at 700°C. This behavior indicates that the carbon species remnants into the pores created by low temperature SDA pyrolysis interact efficiently with CO<sub>2</sub> at low pressures, whereas capture capacity at higher pressures is more favored by the increased pore volume and carbon-free surface created upon higher temperature thermal treatment. Conclusively, if the AlPO<sub>4</sub>-5 adsorbents are to be used for low-pressure CO<sub>2</sub> capture, high thermal activation is not required, as similar capture capacity can be achieved by pyrolysis treatment at significantly lower temperatures, e.g., 240°C, thus saving energy and safeguarding the thermal stability of the adsorbents. The relatively high capacity resulting from such pyrolysis-based activation treatment is attributed to enhanced interaction of CO<sub>2</sub> at low pressures with carbon species that are remnant in the pores upon partial SDA decomposition.

## Effect of Metal Substitution

Ion-substituted AlPO<sub>4</sub>-5 were prepared by incorporating Fe, Mg, Co, and Si into the framework of AlPO<sub>4</sub>-5. Ion substitution in AlPO<sub>4</sub>-5 takes place through various mechanisms depending on the substituting element, with divalent and trivalent ions substituting Al, whereas tetravalent ions such as silicon substitutes predominantly P at low Si content, whereas at higher Si ratios a pair of Si ions substitutes adjacent Al and P ions (Gaber et al., 2020). In the present set of experiments, a water/Al<sub>2</sub>O<sub>3</sub> molar ratio of 100:1 and a metal/Al<sub>2</sub>O<sub>3</sub> ratio of 5:100 were used.

The XRD patterns of the resulting MeAPOs (**Figure 3A**) are in accordance with the AFI structure possessing all the AFI peaks, including the characteristic ones at  $2\theta$  of approximately 20, 22, and 23° that correspond to the reflections from the (210) (002) and (211) crystallographic planes, respectively (Karanikolos et al., 2008; Stoeger et al., 2012; Basina et al., 2018). Furthermore, the materials exhibit high crystallinity as no broad peaks or shoulders and no evidence of secondary crystalline phases/impurities were noticed. A closer look at the XRD patterns reveals that some peaks of the ion substituted AlPOs are not perfectly aligned with those of the AlPO<sub>4</sub>-5. Indeed, **Figure 3B** shows the three characteristic AFI peaks extending between 19 and 23°, which are attributed to the crystallographic (210), (002) and (211) planes where minor shifts are evident. These shifts are attributed to the ion substitution and incorporation into the framework since heteroatoms with different ionic radii are inserted into the lattice substituting Al and/or P. The ionic radius of alumina is 0.53 Å with all substituting metals having larger ionic radii, i.e., Fe: 0.645 Å, Mg: 0.72 Å, and Co: 0.745 Å. Silica possesses an ionic radius is 0.4 Å and has the ability to substitute phosphorus, which has an ionic radius 0.38 Å (SM2 mechanism). Notably, Fe exhibits the biggest expansion along the *c*-dimension. These shifts confirm the successful substitution of the metals into the AlPO framework. Analogous results were reported in our previous work, where AlPO<sub>4</sub>-5 metal substitution resulted in change of lattice parameters (Gaber et al., 2020).

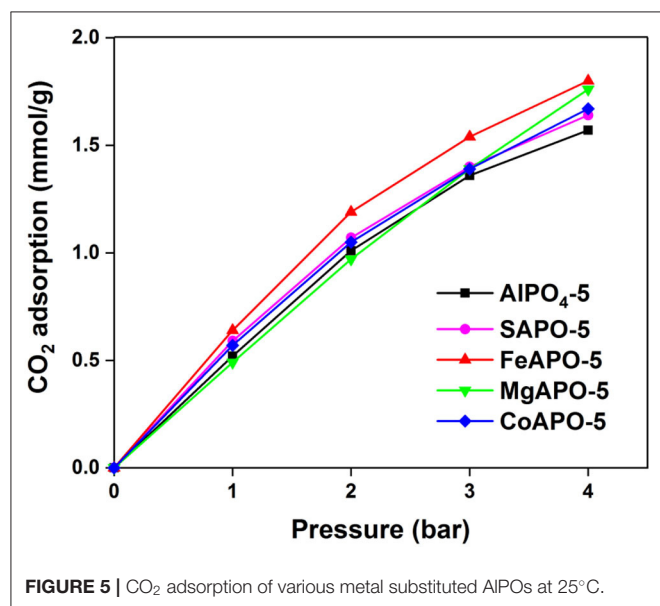
SEM images of calcined AlPO<sub>4</sub>-5 and MeAPO-5 are depicted in **Figure 4**. The materials are comprised of crystalline particles, thus confirming the XRD findings. All images correspond to adsorbents generated from dense reaction mixtures (H<sub>2</sub>O/Al<sub>2</sub>O<sub>3</sub> molar ratio of 100), except **Figure 4c** that corresponds to dilute reaction mixture (H<sub>2</sub>O/Al<sub>2</sub>O<sub>3</sub> molar ratio of 400) and the crystals exhibit columnar morphology. According to the low magnification images, the particles of the materials with

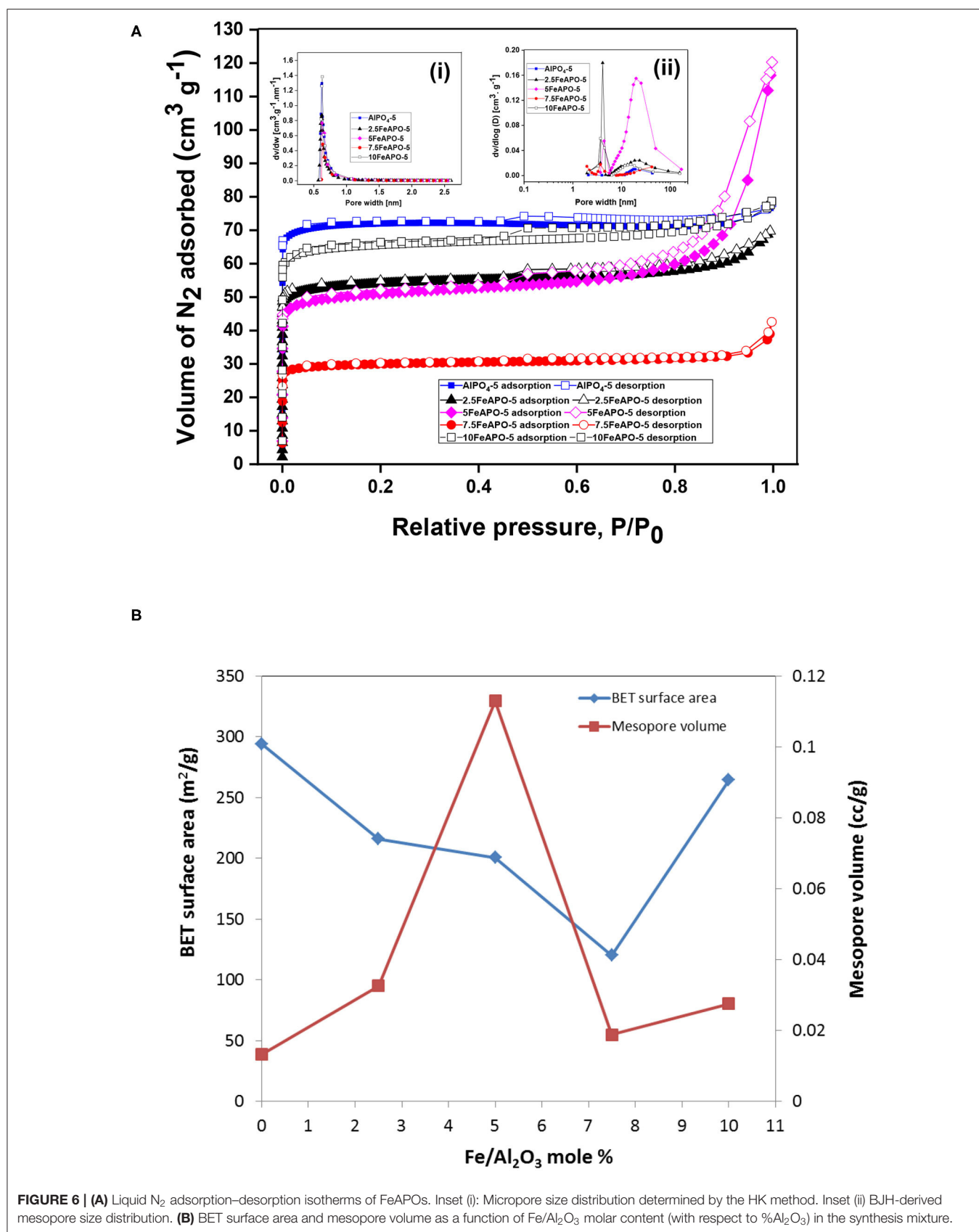
H<sub>2</sub>O/Al<sub>2</sub>O<sub>3</sub> molar ratio of 100 have spherical shape with uniform sizes that range between 20 and 30 μm. In high magnification, it is evident that the spherical particles are agglomerates of flat rectangular-like small crystals. In FeAPO-5 (**Figures 4d,f**), an analogous morphology is observed, whereas it is evident that the crystal aggregates tend to acquire a more hexagonal shape (**Figure 4f**) following the AFI crystal structure. This reveals that the particles in this adsorbent have been formed not by simple physical aggregation of the small individual crystallites, but rather a considerable degree of interaction and coalescence have taken place upon crystal growth.

The MgAPO-5 crystal aggregates (**Figures 4g,h**) exhibit spherical shape with an average particle diameter of 20 μm. The particle size of MgAPO-5 is smaller than that of FeAPO-5, whereas the aggregates seem to have a more perfect spherical shape compared to the hexagonal configuration observed in FeAPO-5. This reveals that interaction and coalescence between the individual small crystallites in MgAPO-5 is lower compared to that in FeAPO-5. CoAPO-5 (**Figures 4i,j**) also mainly consists of spherical particles, but they are quite heterogeneous since some of them have holes at their axis. The majority of SAPO-5 crystals are spherical, but some larger, irregularly shaped aggregates have also formed by further merging of the spherical particles, as shown in **Figures 4k,l**.

The morphology of AlPO<sub>4</sub>-5 prepared at high dilution rate (H<sub>2</sub>O/Al<sub>2</sub>O<sub>3</sub> molar ratio in the synthesis mixture of 400, **Figure 4c**) reveals mainly columnar, hexagonal monocrystals (Cheung et al., 2012; Gaber et al., 2020). This is attributed to the fact that dilution of the reaction gel decreases the nucleation rate (Du et al., 1997), and favors preferential growth along the *c*-axis of the crystals. Indeed, the spheres formed in the samples using dense synthesis mixtures (H<sub>2</sub>O/Al<sub>2</sub>O<sub>3</sub> molar ratio of 100) are comprised of smaller rectangular-like crystals that are tightly interconnected. The progress of crystallization controls the size of the spherical aggregates and prove to be rather homogeneous. FeAPO-5 particles tend to acquire a hexagonal shape in accordance to the AFI morphology compared to the rest of materials grown using dense reaction mixtures, thus indicating a closer interaction and coalescence among the individual flat-like crystallites that comprise each aggregate. This can be correlated to the XRD observations (**Figure 3B**), where FeAPO-5 was shown to exhibit the largest shift in the (002) peak, which may be also partially associated to the interface Fe ions shared among coalesced crystallites. Increasing the dilution slows down the crystallization rate, thus forming hexagonal, rod-like shape crystals following preferential growth along the *c*-axis (Iwasaki et al., 2003; Karanikolos et al., 2008). However, due to slow crystallization, it is possible that these samples may also possess some amorphous areas (Utchariyajit and Wongkasemjit, 2008) and low crystallinity regions.

The CO<sub>2</sub> adsorption results of the metal substituted AlPOs and the parent AlPO<sub>4</sub>-5 are shown in **Figure 5** (data tabulated in **Supplementary Table 2**). Overall, MeAPO-5 samples exhibit higher capacity than the parent AlPO<sub>4</sub>-5 indicating that metal substitution promotes CO<sub>2</sub> adsorption. Among all MeAPO-5 samples, FeAPO-5 exhibits the highest capacity throughout the pressure range tested, reaching a maximum value of 1.8 mmol/g





at 4 bar, which is 15% higher than that of the parent AlPO<sub>4</sub>-5 at the same conditions, owing to the substitution of Al<sup>3+</sup> with Fe<sup>3+</sup> in the lattice. At the lower pressure range of up to 3 bar, the Fe- and Co-substituted analogs exhibit higher capacity than the Mg-substituted one due to the fact that the presence of transition metal elements (Fe and Co) in the lattice tend to enhance the affinity between CO<sub>2</sub> with the inorganic framework compared to alkali earth metals (Mg) and weak metals (Al) (Yu et al., 2018).

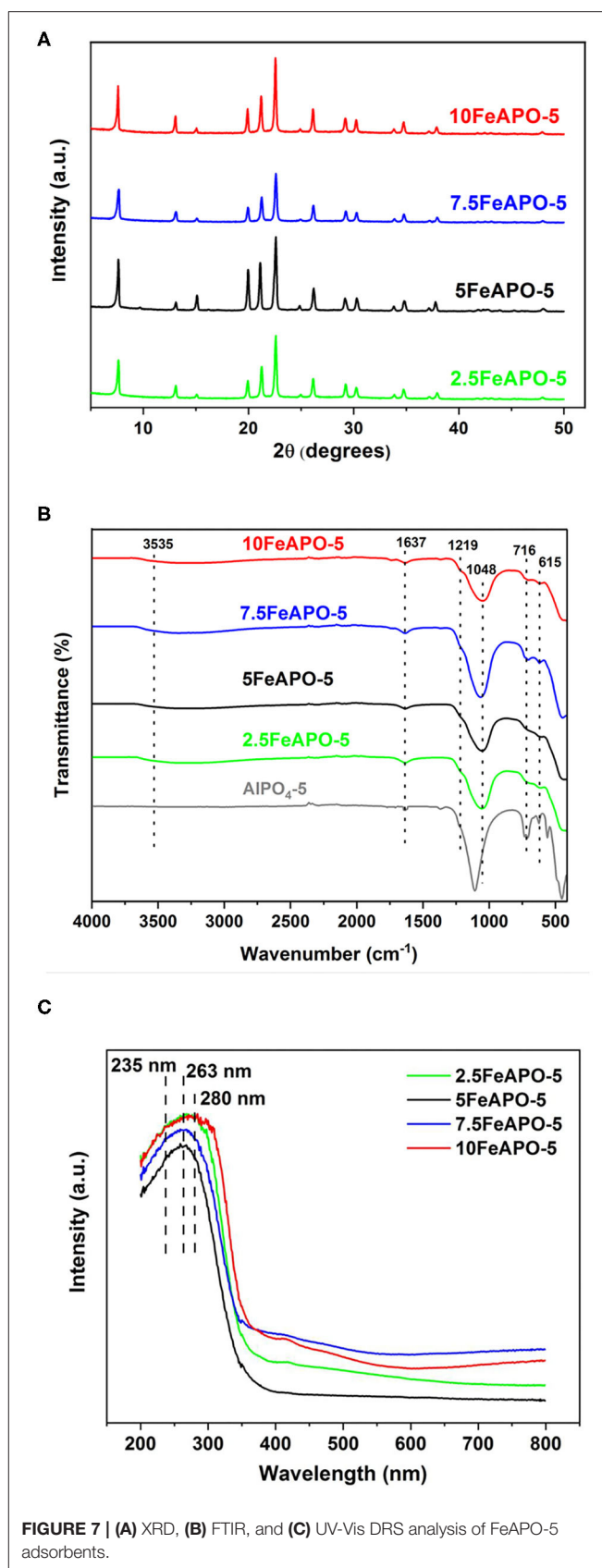
The CO<sub>2</sub> capacity of MgAPO-5 is the lowest at low CO<sub>2</sub> partial pressures even when compared to the parent AlPO<sub>4</sub>-5 adsorbent, whereas at pressures higher than 2.5 bar it displays an increase reaching at 4 bar at an almost same value as that of FeAPO-5. Strong ionic character and bond length in this case (Mg-O 1.969 Å) could influence CO<sub>2</sub> sorption (Caskey et al., 2008; Yazaydin et al., 2009), with a possible clustering effect of CO<sub>2</sub> molecules in the vicinity of Mg within the pores taking place at higher pressures. In addition, diffusion limitations within the pores as well as in the interstitial spaces among the crystallites in each particle agglomerate could be overcome as pressure increases. CoAPO-5 and SAPO-5 contain acidic sites within their framework due to charge imbalance upon ion substitution. Their sorption capacity is slightly higher compared to the parent AlPO<sub>4</sub>-5 adsorbent (by 6% and 4%, respectively). Analogous results were reported using *in situ* IR spectroscopy studies on SAPO-56 adsorbents possessing a high concentration of acid sites (Cheung et al., 2012). Effect of ion substitution on the lattice parameters may play also a role in CO<sub>2</sub> adsorption. The substituting metals have two choices in AlPO<sub>4</sub>-5, i.e., to substitute Al and P positions. In general, Si will preferentially substitute for P, and divalent and trivalent ions will replace Al (Wilson et al., 1982). Substitution by transition metals with higher ionic radius (Fe, Mg, and Co) will generally increase the value of lattice parameters than low ionic radius elements such as Si (Kaneko and Rodríguez-Reinoso, 2019), thus enhancing the CO<sub>2</sub> adsorption capacity.

## Effect of Metal Content

The enhanced CO<sub>2</sub> adsorption capacity of FeAPO-5 compared to all other AlPO samples tested led us to further investigate this material by varying the molar composition of iron in the precursor mixture. An initial molar ratio of Fe/Al<sub>2</sub>O<sub>3</sub> of 5:100 was used as a basis, and a set of materials with three more

**TABLE 2** | Physical properties of FeAPO-5.

Adsorbent	BET surface area (m <sup>2</sup> /g)	Average pore diameter (nm)	Total pore volume (cc/g)	Micropore volume (cc/g)	Mesopore volume (cc/g)
AlPO <sub>4</sub> -5	294.1	1.60	0.1196	0.1063	0.0133
2.5FeAPO-5	215.8	1.98	0.1075	0.0749	0.0326
5FeAPO-5	200.6	3.47	0.1797	0.0668	0.1129
7.5FeAPO-5	120.4	1.93	0.0610	0.0421	0.0189
10FeAPO-5	264.4	1.80	0.1206	0.0930	0.0276



Fe/Al<sub>2</sub>O<sub>3</sub> molar ratios, namely, 2.5:100, 7.5:100, and 10:100, were additionally synthesized and studied.

The liquid N<sub>2</sub> adsorption-desorption isotherms of the FeAPO-5 adsorbents are shown in **Figure 6A**, while the resulting physical and pore properties estimated from BET analysis, BJH, and HK methods are presented in **Table 2**. All adsorbents exhibit a steep nitrogen uptake at a low relative pressure ( $P/P_0$ ) confirming their microporous nature. The adsorbents display a type-IV isotherm with hysteresis loops extending across relative pressures of 0.45 to 0.9, which confirm also the existence of mesopores. Both micropore and mesopore size distributions are shown in insets i and ii, respectively. Among the tested samples, the steepest increase at high relative pressures ( $P/P_0 > 0.8$ ) and the most extensive hysteresis loop was observed for 5FeAPO-5, which are indicative of an extended mesoporous network (**Figure 6B**). According to the micropore size distribution, all-metal substituted samples possess a narrow peak centered at  $\sim 0.7$  nm, which confirms their AFI structure (Karaniolos et al., 2008). From **Table 2**, the BET surface area of FeAPO-5 adsorbents varies from 120 to 264 m<sup>2</sup>/g, the pore volume from 0.06 to 0.18 cc/g, and the average pore diameter from 1.8 to 3.5 nm. The relatively wide ranges observed reveal the considerable affect that the metal incorporation induces to the physical properties of the adsorbents.

To shed more light on the structural effects of the metal content, we also performed XRD, FTIR, and UV-Vis DRS analysis of the FeAPO-5 adsorbents. According to the XRD patterns (**Figure 7A**), the structural integrity of the AFI framework is retained for the whole range of Fe/Al<sub>2</sub>O<sub>3</sub> % molar ratios tested (2.5–10), with no evidence of metal incorporation effects in the AFI crystallinity or appearance of secondary phases/impurities. FTIR spectra are shown in **Figure 7B**. The band at 3,535 cm<sup>-1</sup> is ascribed to -OH functional groups, whereas the bands at 1,219, 716, and 615 cm<sup>-1</sup> are ascribed to the asymmetric and symmetric stretching vibrations of the Al-O-P units (Zhang et al., 2020). Comparing the FeAPO-5 samples with the non-substituted AlPO<sub>4</sub>-5, the band at 562 cm<sup>-1</sup> due to Al-O or P-O bending modes of AlPO<sub>4</sub>-5 framework is significantly suppressed upon Fe incorporation, whereas the band at 1,112 cm<sup>-1</sup>, which corresponds to stretching vibration of Al-O in combination with P-O (Chen and Jehng, 2003), is shifted to lower wavenumber (cm<sup>-1</sup>) values. Comparison among the various FeAPO-5 samples does not reveal any noticeable differences in FTIR bands as to differentiate among the Fe loadings and/or possible Fe segregation. UV-Vis DRS spectra of the Fe-substituted adsorbents are shown in **Figure 7C**. A dominant peak centered at 263 nm is evident for all FeAPO-5 samples with a shoulder at 235 nm attributed to the ligand to metal charge transfer of Fe<sup>3+</sup> in [FeO<sub>4</sub>]<sup>-</sup> tetrahedral geometry (Mohapatra et al., 2002). The intensity of the above band for the unsubstituted AlPO<sub>4</sub>-5 is negligible compared to the iron containing samples (Feng et al., 2016). Notably, for the sample with the highest metal content (10FeAPO-5) the above peak is shifted to higher wavelengths, which is indicative of increased amount of octahedral complexes in extra-framework positions, and the distribution state for the Fe species corresponding to 280 nm in particular can be isolated or clustered (Feng et al., 2016). The broad band between 400

and 500 nm is due to Fe d-d transitions and is also indicative of clustering of iron species (Wei et al., 2008). Notably, the intensity of the above band for the 5FeAPO-5 sample is minimal.

The FeAPO-5 adsorbents exhibit both micropores with an average diameter of  $\sim 0.7$  nm, which is bigger than the kinetic diameter of CO<sub>2</sub> (0.33 nm), thus posing no kinetic restriction for CO<sub>2</sub> adsorption, as well as a relatively extended mesoporous network (**Figure 6A**). In such configuration, at low partial pressure of CO<sub>2</sub>, monolayer adsorption and adsorption on the micropores are anticipated to occur first, whereas mesopores are filled as pressure increases and adsorbate-adsorbate interactions are being enhanced. The CO<sub>2</sub> adsorption capacity of the FeAPO-5 adsorbents with different metal concentrations are shown in **Figure 8** (data also in **Supplementary Table 3**). According to **Figure 6B**, the BET surface area decreases with Fe content until a Fe/Al molar ratio of 7.5:100 and then it increases again. The mesopore volume follows an opposite trend, i.e., it increases with Fe content, exhibits a maximum at Fe/Al ratio of 5:100, and then it decreases. As shown by UV-Vis DRS analysis above, for high metal concentration in the synthesis mixture, a portion of the available Fe forms clusters, and it is not incorporated into the AFI framework as tetrahedrally coordinated ions by substituting Al<sup>3+</sup>. The existence of amorphous Fe<sup>3+</sup> phase for high metal loading has been confirmed also before via various spectroscopic and chemical probe methods (Das et al., 1992). Consequently, the CO<sub>2</sub> adsorption capacity does not exhibit a regular trend as Fe content increases, rather it exhibits a maximum for the sample corresponding to Fe/Al<sub>2</sub>O<sub>3</sub> ratio of 5:100, which exhibits the higher volume of mesopores and the minimum portion of extra-framework or clustered iron as revealed by the UV-Vis analysis. Indeed, the adsorption capacity of 5FeAPO-5 at low pressure (1 bar) is 0.64 mmol/g and at high pressure (4 bar) it becomes 1.8 mmol/g, corresponding to an incremental increase of 1.16 mmol/g from the above low to high pressure

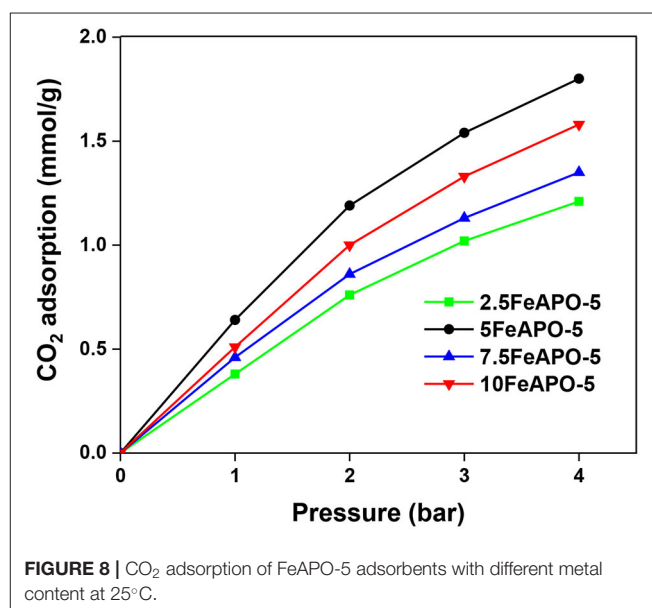
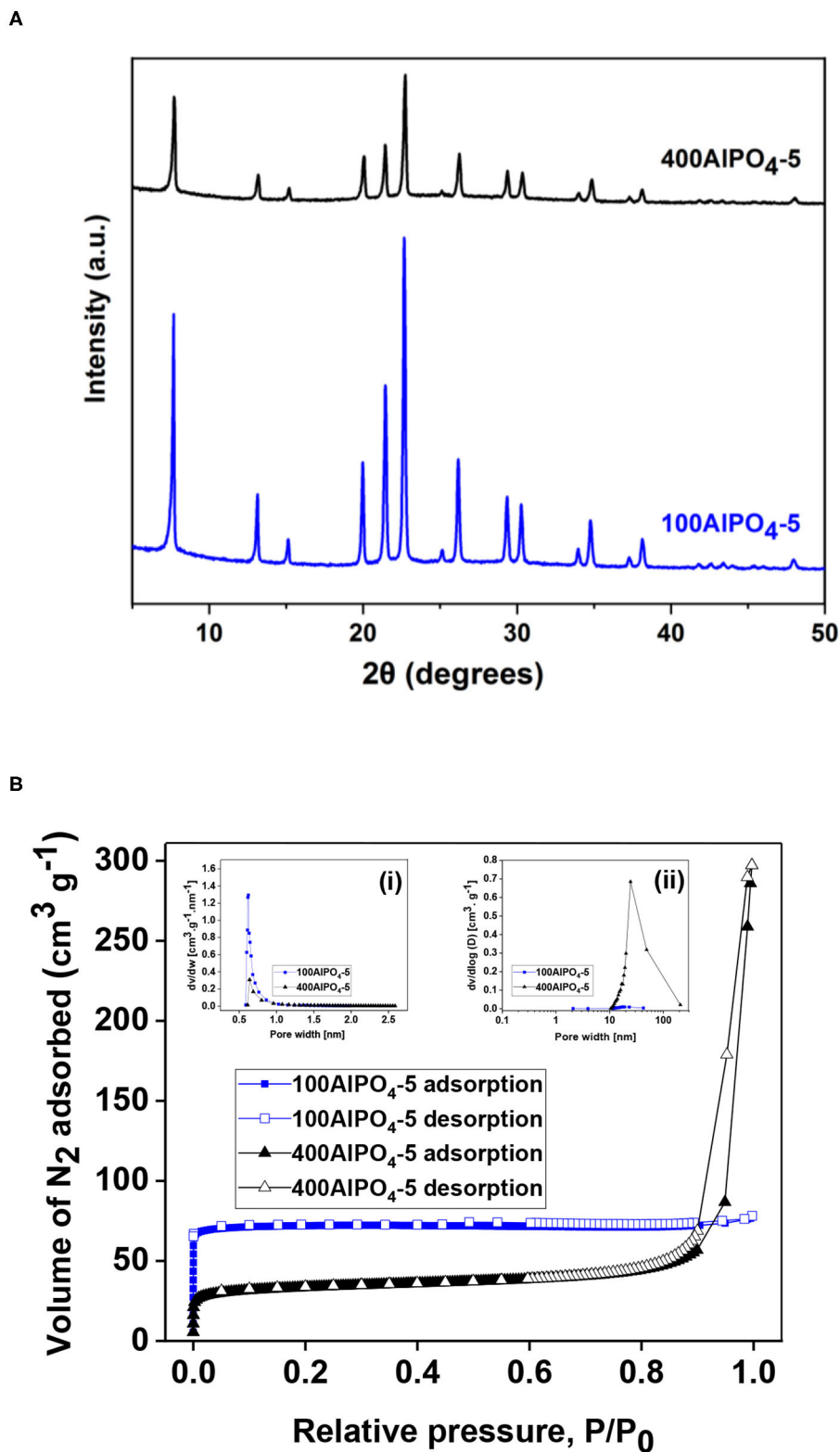


**FIGURE 8** | CO<sub>2</sub> adsorption of FeAPO-5 adsorbents with different metal content at 25°C.



values, which is the highest increment among the FeAPO-5 adsorbents tested. This is attributed to the contribution of mesopores in the adsorption capacity which becomes dominant at higher pressures. Conclusively, Fe incorporation enhances the mesoporosity despite the fact that it decreases the surface area. The latter is more important for relatively low metal content causing a reduction in CO<sub>2</sub> capacity compared to pure AlPO<sub>4</sub>-5, yet as metal content increases, the mesoporosity formation becomes dominant and brings the capacity to higher values than that of the pure AlPO<sub>4</sub>-5 at same conditions. However, for high metal loadings, some Fe prefers to cluster upon growth forming amorphous Fe<sup>3+</sup> phases and/or extra-framework species thus associated to reduced mesoporosity and lower CO<sub>2</sub> capacity.

### Effect of Reaction Mixture Dilution and Associated AlPO<sub>4</sub>-5 Morphology

In our previous work we have shown that a critical parameter that strongly affects crystal morphology upon AlPO<sub>4</sub>-5 growth is the water content in the synthesis mixture (Karanikolos et al., 2008). Specifically, it was demonstrated that dense reaction mixtures favor growth perpendicular to the AFI channels, i.e., along the a-b directions, while diluted reaction mixtures induce preferential growth along the c-direction, i.e., parallel to the

channels. Accordingly, we employed here two different dilutions in the reaction mixture, namely, H<sub>2</sub>O/Al<sub>2</sub>O<sub>3</sub> molar ratio of 100 (sample 100AlPO<sub>4</sub>-5) and 400 (sample 400AlPO<sub>4</sub>-5), which resulted in spherical agglomerates of small flake-like crystallites, and columnar monocrystals, respectively (Figures 4A–C). From XRD analysis (Figure 9A), it is evident that both samples possess the AFI structure, yet the lower-dilution sample displays a higher crystallinity when compared to the high-dilution one.

The liquid N<sub>2</sub> adsorption isotherms and pore size distributions of the 100AlPO<sub>4</sub>-5 and 400AlPO<sub>4</sub>-5 adsorbents are shown in Figure 9B, and the associated physical and porosity properties are presented in Table 3. It is evident that diluted reaction mixtures yield AlPO<sub>4</sub>-5 with lower surface area and micropore volume, yet enhanced mesoporosity. The shape of the isotherms also confirms this observation, as the isotherm of 100AlPO<sub>4</sub>-5 approaches that of type-I revealing a strongly microporous nature with negligible contribution from larger pores, whereas that corresponding to 400AlPO<sub>4</sub>-5 is a type-IV isotherm with a steep rise in adsorption at  $P/P_0 > 0.85$  and an enhanced hysteresis loop revealing capillary condensation in mesopores. Indeed, the surface area drops from 294 to 125 m<sup>2</sup>/g while the mesopore volume increases from 0.0133 to 0.4153 cc/g for the 100AlPO<sub>4</sub>-5 and 400AlPO<sub>4</sub>-5 adsorbents, respectively. The micropore size distribution (Figure 9B, inset ii) is narrow averaging at ~ 0.7 nm for both materials, in accordance to AFI structure, whereas the portion of larger pores is relatively low for 100AlPO<sub>4</sub>-5, and becomes significant for 400AlPO<sub>4</sub>-5, for which an average mesopore width of 25 nm is evidenced from Figure 9B, inset.

The CO<sub>2</sub> adsorption isotherms and associated capacities for the AlPO<sub>4</sub>-5 adsorbents corresponding to low and high dilutions of the reaction mixture are shown in Figure 10. It is evident

TABLE 3 | Physical properties of 100AlPO<sub>4</sub>-5 and 400AlPO<sub>4</sub>-5.

Adsorbent	BET surface area (m <sup>2</sup> /g)	Average pore diameter (nm)	Total pore volume (cc/g)	Micropore volume (cc/g)	Mesopore volume (cc/g)
100AlPO <sub>4</sub> -5	294.1	1.60	0.1196	0.1063	0.0133
400AlPO <sub>4</sub> -5	125.2	13.0	0.4509	0.0356	0.4153

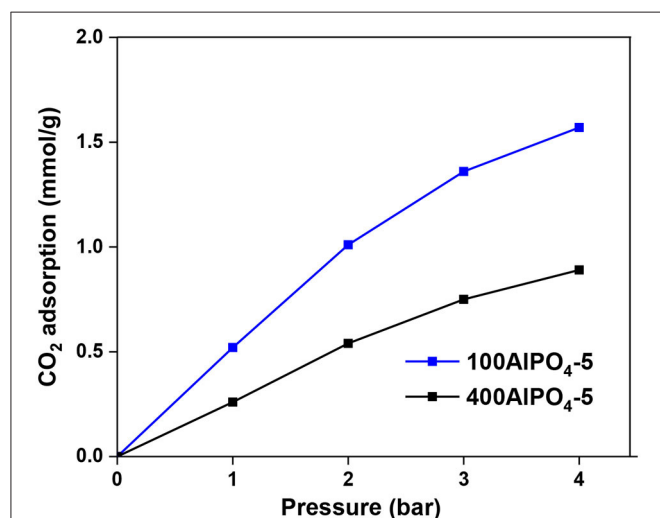


FIGURE 10 | CO<sub>2</sub> adsorption of AlPO<sub>4</sub>-5 adsorbents corresponding to two different reaction mixture dilution rates and associated crystal morphologies at 25°C.

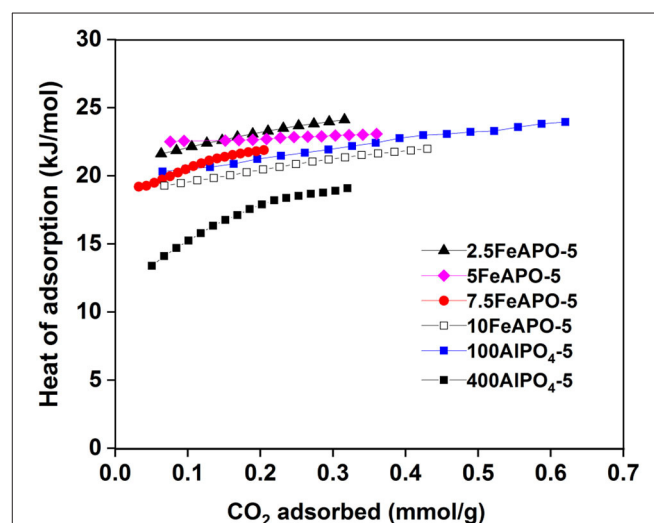


FIGURE 11 | Isothermic heat of adsorption of different AlPO<sub>4</sub>-5 and FeAPO-5 adsorbents.

that dense reaction mixtures (100AlPO<sub>4</sub>-5) yield adsorbents that exhibit higher capacity compared to diluted ones (400AlPO<sub>4</sub>-5). Indeed, 100AlPO<sub>4</sub>-5 exhibits an adsorption capacity of 1.57 mmol CO<sub>2</sub>/g at 4 bar and 25°C, which is almost double than that of 400AlPO<sub>4</sub>-5. As discussed earlier for the Fe-substituted adsorbents, a high mesopore volume is favorable for enhancing CO<sub>2</sub> capacity. Nevertheless, this does not seem to be the case for the non-substituted materials where substituting heteroatoms do not exist. Here, the effect of BET surface area reduction for the adsorbent corresponding to high dilution rate of the reaction mixture is more dominant than the mesoporosity formation, thus causing a decrease in CO<sub>2</sub> capacity compared to the adsorbent originated from dense mixture. In addition, a high average mesopore diameter (25 nm in the case of 400AlPO<sub>4</sub>-5) might decrease the interaction potential, affinity between CO<sub>2</sub>-CO<sub>2</sub>, and retention upon multilayer adsorption.

### Isosteric Heat of Adsorption

The isosteric heat of adsorption concerns the amount of energy that is released when CO<sub>2</sub> adsorbs onto the adsorbent surface at a fixed coverage. Consequently, at least the same amount of energy must be added in order for the CO<sub>2</sub> to be desorbed from the adsorbent upon regeneration. In addition, the isosteric heat of adsorption values provide a quantifiable indicator of the affinity of an adsorbate molecule toward the adsorbent surface. CO<sub>2</sub> adsorption isotherms were collected at three different temperatures in order to calculate the heat of adsorption of the AlPO adsorbents at different CO<sub>2</sub> loadings. The isosteric heat of adsorption values were determined based on the Clausius–Clapeyron equation using the obtained isotherm data, and the results are depicted in **Figure 11**.

The heat of adsorption values for all the studied adsorbents are lower than 25 kJ/mol throughout the tested coverages, which indicates that the mechanism of CO<sub>2</sub> adsorption in these materials is physisorption, in line to the reported literature (Simmons et al., 2011). As such, they hold a high potential for PSA-based capture application as desorption can easily be enabled by pressure swing without the need of thermal regeneration. According to the obtained profiles, the heat of adsorption increases as the CO<sub>2</sub> loading increases for all the studied adsorbents, implying that, as coverage increases, adsorbate–adsorbate (CO<sub>2</sub>-CO<sub>2</sub>) interactions are stronger than adsorbate–adsorbent interactions on CO<sub>2</sub>-philic surface sites. Concerning the Fe-substituted analogs in particular, the ones corresponding to relatively low Fe/Al<sub>2</sub>O<sub>3</sub> molar ratio in the synthesis mixture (2.5:100 and 5:100) exhibit the highest heat of adsorption values compared to the rest of tested adsorbents. This indicates that the incorporated metal enhances the physical binding, a fact that is more pronounced for 5FeAPO-5 at low coverage indicating a stronger CO<sub>2</sub> interaction on the adsorbent surface upon monolayer formation. Notably, the above mentioned adsorbent exhibited the highest uptake compared to the rest of the ion-substituted materials tested as well as to the pure AlPO<sub>4</sub>-5 (**Figures 5, 8**). Furthermore, the heat of adsorption curve of 5FeAPO-5 is almost flat, which is attributed to high crystallinity and homogenous surface with a uniform distribution of the Fe heteroatoms into the framework lattice

that enhance binding. Notably, this adsorbent contains the lowest portion of extra-framework or clustered iron among all FeAPO-5 materials tested (**Figure 7C**). As Fe content in the synthesis mixture increases the heat of adsorption, and thus the CO<sub>2</sub> binding strength with the adsorbent surface decreases, a result that is in agreement to the observed reduced CO<sub>2</sub> adsorption capacity for 7.5FeAPO-5 and 10FeAPO-5, which is attributed to the tendency of the readily available Fe ions at these high metal concentrations to cluster in the synthesis mixture and yield formation of amorphous Fe<sup>3+</sup> phases upon crystal growth (Das et al., 1992), as also discussed above (**Figure 7C**), and/or remain as extra-framework species partially blocking active surface sites.

The low value of heat of adsorption for the 400AlPO<sub>4</sub>-5 adsorbent, which corresponds to diluted reaction mixture, indicates that the morphology and textural and surface properties of this material, including the large pore width, large mesopore volume, and rod-like crystal morphology, promote a very weak binding with the surface, which is in agreement to the low CO<sub>2</sub> adsorption capacity obtained for this material. In addition, the heat of adsorption curve as a function of coverage for this adsorbent exhibits the largest slope among all tested adsorbents for the low coverage range (up to 0.22 mmol/g). This is indicative of the initially weak interaction of CO<sub>2</sub> with the surface and during monolayer adsorption, which becomes stronger as coverage increases due to more dominant adsorbate–adsorbate interactions. At higher coverages (>0.22 mmol/g), the slope becomes lower and almost equalizes with that of the other tested adsorbents.

### CO<sub>2</sub> Adsorption Kinetics

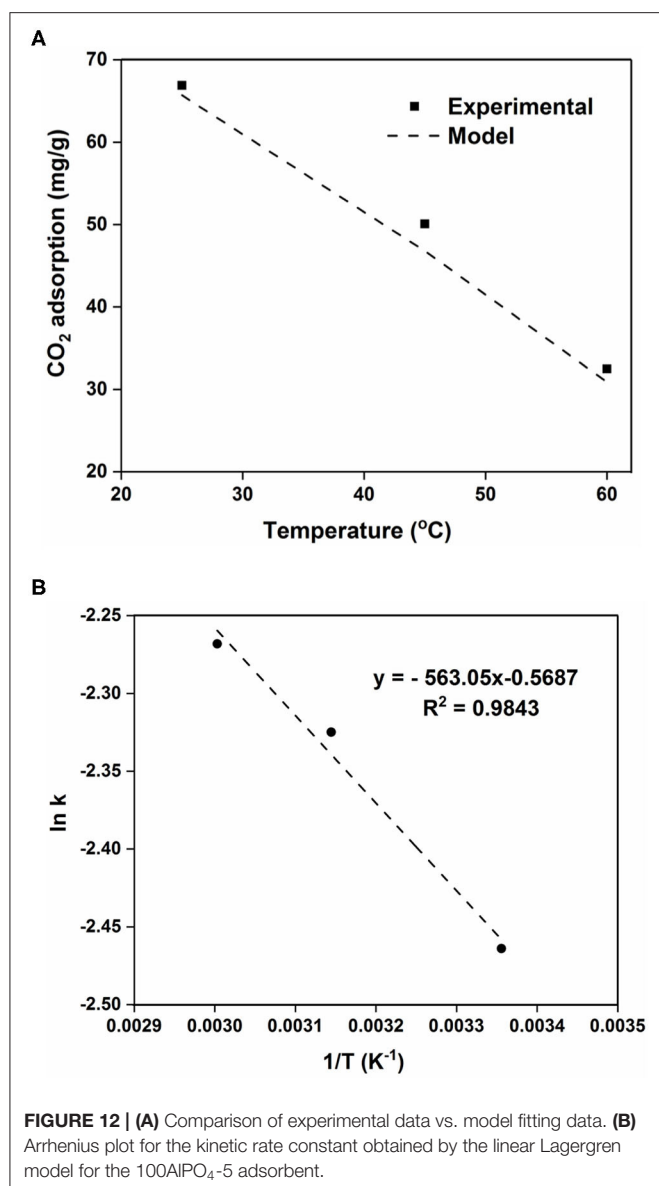
Understanding of the adsorption kinetics of an adsorbent is vital in designing PSA systems (Loganathan et al., 2014). Various adsorption kinetic models have been employed, among which, the pseudo–first-order kinetics or Lagergren model (Liu et al., 2014) is widely used for CO<sub>2</sub> adsorption. The pseudo–first-order equation models a reversible interaction between adsorbent and adsorbate. This is suitable for describing the physical adsorption of CO<sub>2</sub> on solid adsorbents (Serna-Guerrero and Sayari, 2010; Loganathan et al., 2014). The pseudo–first-order model is governed by Equation (1):

$$\frac{dq_t}{dt} = k(q_e - q_t) \quad (1)$$

where  $q_e$  and  $q_t$  (mg/g) represent the amount of CO<sub>2</sub> adsorbed at equilibrium and at a given time “ $t$ ”, respectively, and  $k$  (min<sup>-1</sup>) is the first order rate constant. The relevant boundary conditions are BC1:  $t = 0, q_t = 0$  and BC2:  $t = \infty, q_t = q_e$ . Applying

**TABLE 4** | Adsorption rate constant ( $k$ ) at different temperatures and up to 4 bar for 100AlPO<sub>4</sub>-5.

Temperature (°C)	Constant rate $k$ (min <sup>-1</sup> )
25	0.0851
45	0.0978
60	0.1035



the above boundary conditions to Equation (1) while solving the aforementioned differential equation leads to Equation (2).

$$\log(q_e - q_t) = \log(q_e) - \left(\frac{k}{2.303}\right)t \quad (2)$$

The higher CO<sub>2</sub> adsorption capacity and rate of the 100AlPO<sub>4</sub>-5 adsorbent compared to the 400AlPO<sub>4</sub>-5 analog, as confirmed by both equilibrium data at various pressures (Figure 10), and kinetic data up to 4 bar (Supplementary Figure 3) led us to further investigate the kinetic behavior of this adsorbent by conducting adsorption experiments at three different temperatures, i.e., 25, 45, and 60°C up to a pressure of 4 bar (Supplementary Table 5 and Supplementary Figure 4). The CO<sub>2</sub> adsorption capacity decreases as temperature increases confirming the physisorption mechanism. In order

to calculate the adsorption rate constant  $k$  for the three different temperatures, the adsorption data at the different temperatures were used to plot  $\log(q_e - q_t)$  vs.  $t/2.303$  (Supplementary Figure 5). The resulting linear fit slope is the adsorption rate constant ( $k$ ), and the  $y$ -intercept is  $\log q_e$  (Liu and Shen, 2008; Liu et al., 2014). The adsorption rate constant increases as temperature increases (Table 4) yet with relatively slight differences indicating that the adsorption of CO<sub>2</sub> on AlPO<sub>4</sub>-5 is rather thermodynamically limited. The equilibrium adsorption capacity ( $q_e$ ) was also calculated from the pseudo-first-order model and compared with the experimentally measured one (Supplementary Table 5). The model predicted the equilibrium adsorption capacity with an average relative error of 1.8–6.5%, and the value of the correlation coefficient ( $R^2$ ) of the model is around 0.98. Thus, the pseudo-first-order model proves to be qualitatively and quantitatively suitable for modeling of CO<sub>2</sub> adsorption kinetics of the studied AlPO<sub>4</sub>-5 adsorbents as shown Figure 12A.

The temperature dependence of rate constant ( $k$ ) can be described by the Arrhenius equation (Equation 3), where  $A$  is the pre-exponential factor,  $E$  is the activation energy,  $R$  is the universal gas constant, and  $T$  is the temperature in absolute units.

$$k = Ae^{-\left(\frac{E}{RT}\right)} \quad (3)$$

The plot of  $\ln(k)$  vs.  $1/T$  (Figure 12B) exhibits a linear profile, as anticipated from the linearized form of the Arrhenius equation. From the obtained slope, the activation energy for the CO<sub>2</sub> adsorption on 100AlPO<sub>4</sub>-5 at 4 bar was calculated to be 4.7 kJ/mol. The obtained activation energy value is in close agreement to the reported values of CO<sub>2</sub> adsorption on activated carbon and Zeolite 13X, where activation energies of 3.9 and 4.8 kJ/mol, respectively, were estimated up to CO<sub>2</sub> pressure of 3 bar (Zhang et al., 2010).

## CONCLUSIONS

Effects of metal substitution, synthesis mixture composition and associated morphology manipulation, and activation procedure on AlPO<sub>4</sub>-5 were studied for CO<sub>2</sub> adsorption. Activation by calcination in air at high temperature was found to completely open up the pores resulting in higher CO<sub>2</sub> capacity compared to calcination at lower temperatures. Yet, upon activation by pyrolysis in inert atmosphere, low temperature (240°C) treatment enhanced CO<sub>2</sub> interaction with the surface at low pressures (up to 1 bar) due to the existence of remnant carbon species in the pores from the partial decomposition of the SDA. Ion substitution by Fe, Mg, Co, and Si induced changes in lattice parameters and morphology, whereas the Fe-substituted adsorbents exhibited the highest capacity compared to the rest of metal-substituted analogs. Parametric variation of the Fe content in the synthesis mixture revealed that, at relatively low metal concentrations, mesopore volume increases and microporosity and BET surface area decrease with metal content. At these conditions, the strong interaction of CO<sub>2</sub> with the framework Fe and the adsorbate-adsorbate

interactions in the formed mesopores increased the CO<sub>2</sub> capacity. For high metal concentrations, some Fe prefers to cluster upon growth forming amorphous Fe<sup>3+</sup> phases and/or extra-framework species, thus resulting in reduced mesoporosity and lower CO<sub>2</sub> capacity. Dense reaction mixtures yielded AlPO<sub>4</sub>-5 consisting of spherical agglomerates of 2D-like crystallites that were almost exclusively microporous in nature, whereas diluted reaction mixtures resulted in crystals of columnar morphology exhibiting significant mesoporosity. In contrast to the metal-substituted analogs and thus in the absence of metal-CO<sub>2</sub> interactions, the microporosity and high surface area of the AlPO<sub>4</sub>-5 adsorbents corresponding to dense reaction mixtures were dominant factors compared to the enhanced mesoporosity of the ones grown from diluted mixtures, thus yielding higher CO<sub>2</sub> capacity for the former materials.

The isosteric heat of adsorption values for all the studied adsorbents were lower than 25 kJ/mol indicating that the mechanism of CO<sub>2</sub> adsorption is physisorption, which is suitable for PSA application. The Fe-substituted analog corresponding to a Fe/Al<sub>2</sub>O<sub>3</sub> molar ratio in the reaction mixture of 5:100 exhibited the highest heat of adsorption at low coverage, indicating affinity and stronger physical binding of CO<sub>2</sub> with the framework-incorporated Fe. Notably, this adsorbent exhibited the lowest portion of extra-framework or clustered iron. Kinetic analysis revealed that a pseudo-first-order model could describe well the CO<sub>2</sub> adsorption kinetics of the AlPO<sub>4</sub>-5 adsorbents, with an activation energy of 4.7 kJ/mol at 4 bar and adsorption rate constants increasing with temperature, yet with rather slight differences. AlPO<sub>4</sub>-5-based adsorbents, though they exhibit rather moderate capacities, they are robust, thermally and chemically stable materials, they exhibit low heat of adsorption, thus potential for PSA application, and limited hydrophilicity compared to classical zeolites that makes them important for CO<sub>2</sub> capture from wet streams. The parametric investigation performed in this work sheds light on main optimization factors and

paves the way for further studies toward implementation at industrial scale.

## DATA AVAILABILITY STATEMENT

All datasets generated for this study are included in the article/**Supplementary Material**.

## AUTHOR CONTRIBUTIONS

AP performed the synthesis/growth, characterization of the adsorbents, and drafted part of the manuscript. KR performed the CO<sub>2</sub> evaluation and drafted part of the manuscript. DK edited the manuscript and contributed in the supervision of AP. DR edited the manuscript and contributed in the supervision of the activities. YA contributed in the supervision of the activities, provided feedback and ideas, contributed in the design of the experiments, and edited the manuscript. GK set up and designed the project, attracted the funding, supervised the activities, and drafted/edited the manuscript. All authors contributed to the article and approved the submitted version.

## ACKNOWLEDGMENTS

The authors acknowledge support by the R&D division of the Abu Dhabi National Oil Company (ADNOC, project RDProj.018-GP) and Khalifa University (Award No. CIRA-2020-093). We thank Ms. Abeer Ali Nasser Al Yafeai, Ms. Tharalekshmy Anjana, and Ms. Dina Ali Gaber for assistance with SEM, XRD, and UV-Vis characterizations, respectively.

## SUPPLEMENTARY MATERIAL

The Supplementary Material for this article can be found online at: <https://www.frontiersin.org/articles/10.3389/fchem.2020.568669/full#supplementary-material>

## REFERENCES

- Basina, G., AlShami, D., Polychronopoulou, K., Tzitzios, V., Balasubramanian, V., Dawaymeh, F., et al. (2018). Hierarchical AlPO<sub>4</sub>-5 and SAPO-5 microporous molecular sieves with mesoporous connectivity for water sorption applications. *Surface Coat. Technol.* 353, 378–386. doi: 10.1016/j.surfcoat.2018.08.083
- Carmine, C. (2012). The fascinating story of porous materials. *Curr. Phys. Chem.* 2, 126–135. doi: 10.2174/1877946811202020126
- Caskey, S. R., Wong-Foy, A. G., and Matzger, A. J. (2008). Dramatic tuning of carbon dioxide uptake via metal substitution in a coordination polymer with cylindrical pores. *J. Am. Chem. Soc.* 130, 10870–10871. doi: 10.1021/ja8036096
- Chen, C.-M., and Jehng, J.-M. (2003). Effect of synthesis pH and H<sub>2</sub>O molar ratio on the structure and morphology of aluminum phosphate (AlPO<sub>4</sub>-5) molecular sieves. *Catal. Lett.* 85, 73–80. doi: 10.1023/A:1022120824681
- Cheung, O., Liu, Q., Bacsik, Z., and Hedin, N. (2012). Silicoaluminophosphates as CO<sub>2</sub> sorbents. *Microp. Mesop. Mater.* 156, 90–96. doi: 10.1016/j.micromeso.2012.02.003
- Choi, S., Drese, J. H., and Jones, C. W. (2009). Adsorbent materials for carbon dioxide capture from large anthropogenic point sources. *ChemSusChem* 2, 796–854. doi: 10.1002/cssc.200900036
- Chou, C. T., and Chen, C. Y. (2004). Carbon dioxide recovery by vacuum swing adsorption. *Sep. Purif. Technol.* 39, 51–65. doi: 10.1016/j.seppur.2003.12.009
- Chue, K. T., Kim, J. N., Yoo, Y. J., Cho, S. H., and Yang, R. T. (1995). Comparison of activated carbon and zeolite 13X for CO<sub>2</sub> recovery from flue gas by pressure swing adsorption. *Indu. Eng. Chem. Res.* 34, 591–598. doi: 10.1021/ie00041a020
- Corma, A. (2003). State of the art and future challenges of zeolites as catalysts. *J. Catal.* 216, 298–312. doi: 10.1016/S0021-9517(02)00132-X
- Cundy, C. S., and Cox, P. A. (2003). The hydrothermal synthesis of zeolites: history and development from the earliest days to the present time. *Chem. Rev.* 103, 663–702. doi: 10.1021/cr020060i
- Das, J., Satyanaryana, C. V. V., Chakrabarty, D. K., Piramanayagam, S. N., and Shringi, S. N. (1992). Substitution of Al in the AlPO<sub>4</sub>-5 and AlPO<sub>4</sub>-11 frameworks by Si and Fe: a study by Mössbauer, magic-angle-spinning nuclear magnetic resonance and electron paramagnetic resonance spectroscopies and chemical probes. *J. Chem. Soc. Faraday Transact.* 88, 3255–3261. doi: 10.1039/FT9928803255

- Delgado, J. A., Águeda, V. I., Uguina MA, Sotelo, J. L., and Fernández, P. (2013). Adsorption and diffusion of nitrogen, methane and carbon dioxide in aluminophosphate molecular sieve AlPO<sub>4</sub>-11. *Adsorption* 19, 407–422. doi: 10.1007/s10450-012-9463-6
- Du, H., Fang, M., Xu, W., Meng, X., and Pang, W. (1997). Preparation by microwave irradiation of nanometre-sized AlPO<sub>4</sub>-5 molecular sieve. *J. Mater. Chem.* 7, 551–555. doi: 10.1039/a606132j
- Feng, B., Li, J., Zhu, X., Guo, Q., Zhang, W., Wen, G., et al. (2016). The state of iron sites in the calcined FeAlPO<sub>4</sub>-5 and its tuning to the property of microporous AlPO<sub>4</sub>-5 molecular sieve. *Catal. Today* 263, 91–97. doi: 10.1016/j.cattod.2015.06.022
- Gaber, S. A., Dawaymeh, F., Gaber, D. A., Basina, G., Ismail, I., Tharakshmy, A., et al. (2020). Combined DFT and experimental investigation on ion isomorphous substitution of aluminophosphate microporous crystals. *Microp. Mesop. Mater.* 294:109859. doi: 10.1016/j.micromeso.2019.109859
- Guo, Z., Guo, C., Jin, Q., Li, B., and Ding, D. (2005). Synthesis and structure of large AlPO<sub>4</sub>-5 crystals. *J. Porous Mater.* 12, 29–33. doi: 10.1007/s10934-005-5230-3
- Haszeldine, R. S. (2009). Carbon capture and storage: how green can black be? *Science* 325, 1647–1652. doi: 10.1126/science.1172246
- IEA (2016). *CO<sub>2</sub> Emissions from Fuel Combustion*. Paris: IEA.
- Iwasaki, A., Sano, T., Kodaira, T., and Kiyozumi, Y. (2003). Growth behaviors of AFI type crystals. *Microp. Mesop. Mater.* 64, 145–153. doi: 10.1016/S1387-1811(03)00462-1
- Kaneko, K., and Rodríguez-Reinoso, F. (2019). *Nanoporous Materials for Gas Storage*. New Jersey, NJ: Springer. doi: 10.1007/978-981-13-3504-4
- Karanikolos, G. N., Garcia, H., Corma, A., and Tsapatsis, M. (2008). Growth of AlPO<sub>4</sub>-5 and CoAPO-5 films from amorphous seeds. *Microp. Mesop. Mater.* 115, 11–22. doi: 10.1016/j.micromeso.2007.11.051
- Kontos, A. G., Likodimos, V., Veziri, C. M., Kouvelos, E., Moustakas, N., Karanikolos, G. N., et al. (2014). CO<sub>2</sub> captured in zeolitic imidazolate frameworks: Raman spectroscopic analysis of uptake and host-guest interactions. *ChemSusChem* 7, 1696–1702. doi: 10.1002/cssc.201301323
- Kueh, B., Kapsi, M., Veziri, C. M., Athanasekou, C., Pilatos, G., Reddy, K. S. K., et al. (2018). Asphaltene-derived activated carbon and carbon nanotube membranes for CO<sub>2</sub> separation. *Energy Fuels* 32, 11718–11730. doi: 10.1021/acs.energyfuels.8b02913
- Labropoulos, A., Veziri, C., Kapsi, M., Pilatos, G., Likodimos, V., Tsapatsis, M., et al. (2015). Carbon nanotube selective membranes with subnanometer, vertically aligned pores, and enhanced gas transport properties. *Chem. Mater.* 27, 8198–8210. doi: 10.1021/acs.chemmater.5b01946
- Liu, Q., Cheung, N. C., Garcia-Bennett, A. E., and Hedin, N. (2011). Aluminophosphates for CO<sub>2</sub> separation. *ChemSusChem* 4, 91–97. doi: 10.1002/cssc.201000256
- Liu, Q., Shi, J., Zheng, S., Tao, M., He, Y., and Shi, Y. (2014). Kinetics studies of CO<sub>2</sub> adsorption/desorption on amine-functionalized multiwalled carbon nanotubes. *Indus. Eng. Chem. Res.* 53, 11677–11683. doi: 10.1021/ie502009n
- Liu, Y., and Shen, L. (2008). From langmuir kinetics to first- and second-order rate equations for adsorption. *Langmuir* 24, 11625–11630. doi: 10.1021/la801839b
- Loganathan, S., Tikmani, M., Edubilli, S., Mishra, A., and Ghoshal, A. K. (2014). CO<sub>2</sub> adsorption kinetics on mesoporous silica under wide range of pressure and temperature. *Chem. Eng. J.* 256, 1–8. doi: 10.1016/j.ccej.2014.06.091
- Metz, B., Davidson, O., De Coninck, H., Loos, M., and Meyer, L. (2005). *IPCC Special Report on Carbon Dioxide Capture and Storage*, in: *Intergovernmental Panel on Climate Change*. Geneva: Working Group III.
- Mohapatra, S. K., Sahoo, B., Keune, W., and Selvam, P. (2002). Synthesis, characterization and catalytic properties of trivalent iron substituted hexagonal mesoporous aluminophosphates. *Chem. Commun.* 14, 1466–1467. doi: 10.1039/b204215k
- Musyoka, N. M., Petrik, L. F., Hums, E., Kuhnt, A., and Schwieger, W. (2015). Thermal stability studies of zeolites A and X synthesized from South African coal fly ash. *Res. Chem. Intermed.* 41, 575–582. doi: 10.1007/s11164-013-1211-3
- Peri, J. B. (1971). Surface chemistry of AlPO<sub>4</sub>—a mixed oxide of Al and P. *Discuss. Faraday Soc.* 52, 55–65. doi: 10.1039/DF9715200055
- Pilatos, G., Vermisoglou, E. C., Romanos, G. E., Karanikolos, G. N., Boukos, N., Likodimos, V., et al. (2010). A closer look inside nanotubes: Pore structure evaluation of anodized alumina templated carbon nanotube membranes through adsorption and permeability studies. *Adv. Funct. Mater.* 20, 2500–2510. doi: 10.1002/adfm.200901429
- Pokhrel, J., Bhorina, N., Wu, C., Reddy, K. S. K., Margetis, H., Anastasiou, S., et al. (2018). Cu- and Zr-based metal organic frameworks and their composites with graphene oxide for capture of acid gases at ambient temperature. *J. Solid State Chem.* 266, 233–243. doi: 10.1016/j.jssc.2018.07.022
- Rajic, N., and Kaucic, V. (2002). *Molecular Sieves: Aluminophosphates*, in: *Encyclopedia of Catalysis*. Singapore: John Wiley & Sons, Inc., doi: 10.1002/0471227617.eoc151
- Resnik, K. P., Yeh, J. T., and Pennline, H. W. (2004). Aqua ammonia process for simultaneous removal of CO<sub>2</sub>, SO<sub>2</sub> and NO<sub>x</sub>. *Int. J. Environ. Technol. Manage.* 4, 89–104. doi: 10.1504/IJETM.2004.004634
- Sawant, S. Y., Munusamy, K., Somani, R. S., John, M., Newalkar, B. L., and Bajaj, H. C. (2017). Precursor suitability and pilot scale production of super activated carbon for greenhouse gas adsorption and fuel gas storage. *Chem. Eng. J.* 315, 415–425. doi: 10.1016/j.ccej.2017.01.037
- Sayari, A., Belmabkhout, Y., and Serna-Guerrero, R. (2011). Flue gas treatment via CO<sub>2</sub> adsorption. *Chem. Eng. J.* 171, 760–774. doi: 10.1016/j.ccej.2011.02.007
- Schlegel, M. C., Grzimek, V., Guenther, G., Svetogorov, R., Veziri, C. M., Kapsi, M., et al. (2018). Explaining water adsorption in one-dimensional channels in AlPO<sub>4</sub>-5 on molecular scale. *Microp. Mesop. Mater.* 304:109201. doi: 10.1016/j.micromeso.2018.11.025
- Serna-Guerrero, R., and Sayari, A. (2010). Modeling adsorption of CO<sub>2</sub> on amine-functionalized mesoporous silica. 2: kinetics and breakthrough curves. *Chem. Eng. J.* 161, 182–190. doi: 10.1016/j.ccej.2010.04.042
- Simmons, J. M., Wu, H., Zhou, W., and Yildirim, T. (2011). Carbon capture in metal-organic frameworks—a comparative study. *Energy Environ. Sci.* 4, 2177–2185. doi: 10.1039/c0ee00700e
- Sircar, S., and Golden, T. C. (1995). Isothermal and isobaric desorption of carbon dioxide by purge. *Indus. Eng. Chem. Res.* 34, 2881–2888. doi: 10.1021/ie00047a042
- Siriwardane, R. V., Shen, M.-S., Fisher, E. P., and Poston, J. A. (2001). Adsorption of CO<sub>2</sub> on molecular sieves and activated carbon. *Energy Fuels* 15, 279–284. doi: 10.1021/ef000241s
- Stoeger, J. A., Veziri, C. M., Palomino, M., Corma, A., Kanellopoulos, N. K., Tsapatsis, M., et al. (2012). On stability and performance of highly c-oriented columnar AlPO<sub>4</sub>-5 and CoAPO-5 membranes. *Microp. Mesop. Mater.* 147, 286–294. doi: 10.1016/j.micromeso.2011.06.028
- Tabish, A., Varghese, A. M., Wahab, M. A., and Karanikolos, G. N. (2020). Perovskites in the energy grid and CO<sub>2</sub> conversion: current context and future directions. *Catalysts* 10:95. doi: 10.3390/catal10010095
- Tang, Z. K., Sun, H. D., Wang, J., Chen, J., and Li, G. (1998). Mono-sized single-wall carbon nanotubes formed in channels of AlPO<sub>4</sub>-5 single crystal. *Appl. Phys. Lett.* 73, 2287–2289. doi: 10.1063/1.121704
- Utcharyajit, K., and Wongkasemjit, S. (2008). Structural aspects of mesoporous AlPO<sub>4</sub>-5 (AFI) zeotype using microwave radiation and aluminatane precursor. *Microp. Mesop. Mater.* 114, 175–184. doi: 10.1016/j.micromeso.2008.01.002
- Varghese, A. M., and Karanikolos, G. N. (2020). CO<sub>2</sub> capture adsorbents functionalized by amine-bearing polymers: A review. *Int. J. Greenhouse Gas Control* 96:103005. doi: 10.1016/j.ijggc.2020.103005
- Wan, Y., Williams, C. D., Duke, C. V. A., and Cox, J. J. (2000). Systematic studies on the effect of water content on the synthesis, crystallisation, conversion and morphology of AlPO<sub>4</sub>-5 molecular sieve. *J. Mater. Chem.* 10, 2857–2862. doi: 10.1039/b006127l
- Wei, W., Mouljin, J. A., and Mul, G. (2008). Effect of steaming of iron containing AlPO<sub>4</sub>-5 on the structure and activity in N<sub>2</sub>O decomposition. *Microp. Mesop. Mater.* 112, 193–201. doi: 10.1016/j.micromeso.2007.09.030
- Wilson, S. T., Lok, B. M., Messina, C. A., Cannan, T. R., and Flanigen, E. M. (1982). Aluminophosphate molecular sieves: a new class of microporous crystalline inorganic solids. *J. Am. Chem. Soc.* 104, 1146–1147. doi: 10.1021/ja00368a062
- Yazaydin, A. Ö., Snurr, R. Q., Park, T.-H., Koh, K., Liu, J., LeVan, M. D., et al. (2009). Screening of metal-organic frameworks for carbon dioxide capture from flue gas using a combined experimental and modeling approach. *J. Am. Chem. Soc.* 131, 18198–18199. doi: 10.1021/ja9057234
- Yu, Y., Li, X., Krishna, R., Liu, Y., Cui, Y., Du, J., et al. (2018). Enhancing CO<sub>2</sub> adsorption and separation properties of aluminophosphate zeolites

- by isomorphous heteroatom substitutions. *ACS Appl. Mater. Interfaces*. 10, 43570–43577. doi: 10.1021/acsami.8b11235
- Zhang, S., Cui, M., Zheng, J., and Meng, C. (2020). Insights of the crystallization process of AlPO<sub>4</sub>-5 using hexamethyleneimine as template. *Solid State Sci.* 105:106291. doi: 10.1016/j.solidstatesciences.2020.106291
- Zhang, Z., Zhang, W., Chen, X., Xia, Q., and Li, Z. (2010). Adsorption of CO<sub>2</sub> on zeolite 13X and activated carbon with higher surface area. *Separat. Sci. Technol.* 45, 710–719. doi: 10.1080/01496390903571192
- Zhao, X.-X., Xu, X.-L., Sun, L.-B., Zhang, L. L., and Liu, X.-Q. (2009). Adsorption behavior of carbon dioxide and methane on AlPO<sub>4</sub>-14: a neutral molecular sieve. *Energy Fuels* 23, 1534–1538. doi: 10.1021/ef8008635

**Conflict of Interest:** The authors declare that the research was conducted in the absence of any commercial or financial relationships that could be construed as a potential conflict of interest.

Copyright © 2020 Papageorgiou, Reddy, Karonis, Reinalda, Al Wahedi and Karanikolos. This is an open-access article distributed under the terms of the Creative Commons Attribution License (CC BY). The use, distribution or reproduction in other forums is permitted, provided the original author(s) and the copyright owner(s) are credited and that the original publication in this journal is cited, in accordance with accepted academic practice. No use, distribution or reproduction is permitted which does not comply with these terms.